



HAL
open science

Main water pathways in cultivated clayey calcisols in molassic hills in southwestern France: Toward spatialization of soil waterlogging

Benjamin Trochon, Vincent Bustillo, Laurent Caner, Sylvain Pasquet, Virginie Suc, Franck Granouillac, Anne Probst, Jean-Luc Probst, Tiphaine Tallec, Maritxu Guiresse

► To cite this version:

Benjamin Trochon, Vincent Bustillo, Laurent Caner, Sylvain Pasquet, Virginie Suc, et al.. Main water pathways in cultivated clayey calcisols in molassic hills in southwestern France: Toward spatialization of soil waterlogging. *Vadose Zone Journal*, 2023, 22 (5), pp.e20272. 10.1002/vzj2.20272 . hal-04317713

HAL Id: hal-04317713

<https://hal.science/hal-04317713v1>



Submitted on 1 Dec 2023

HAL is a multi-disciplinary open access archive for the deposit and dissemination of scientific research documents, whether they are published or not. The documents may come from teaching and research institutions in France or abroad, or from public or private research centers.

L'archive ouverte pluridisciplinaire **HAL**, est destinée au dépôt et à la diffusion de documents scientifiques de niveau recherche, publiés ou non, émanant des établissements d'enseignement et de recherche français ou étrangers, des laboratoires publics ou privés.

ORIGINAL ARTICLE

Main water pathways in cultivated clayey calcisols in molassic hills in southwestern France: Toward spatialization of soil waterlogging

Benjamin Trochon¹ | Vincent Bustillo² | Laurent Caner³ | Sylvain Pasquet⁴ |
 Virginie Suc¹ | Franck Granouillac^{1,2} | Anne Probst¹ | Jean-Luc Probst¹  |
 Tiphaine Tallec² | Maritxu Guisresse¹ 

¹Laboratoire écologie fonctionnelle et environnement, University of Toulouse, CNRS, INPT, UPS, Toulouse, France

²CESBIO, University of Toulouse, CNES/CNRS/INRAE/IRD/UPS, Toulouse, France

³University of Poitiers, IC2MP-HydrASA UMR 7285, Poitiers, France

⁴Institut de physique du globe de Paris, CNRS, University of Paris, Paris, France

Correspondence

Maritxu Guisresse, LEFE (INP-ENSAT), Avenue de l'agrobiopole, Auzeville Tolosane, Toulouse 31326, France.
 Email: guisresse@ensat.fr

Assigned to Associate Editor Jean Caron.

Funding information

French Ministry of Agriculture and Occitanie Region subsidies

Abstract

Local waterlogging often occurs on the steep slopes of clayey–calcareous soils in southwestern France, causing nutrients and pollutants transfer to the river bodies and reduced ecosystems services. These soils developed in the Miocene molassic hill formation and are generally impermeable with abundant traces of hydromorphy and heterogenous spatial distribution. This article aims to describe the hydrological functioning of these soils, based on a cross analysis of pedological, hydrological, and geophysical characterizations. Our experimental site is the catchment area located in Auradé (southwestern France). Here, we analyze the flows at the outlet of the studied watershed together with piezometric and climatic monitoring from September 2020 to September 2021. We show that the hydrological year is divided into three phases: first, a soil recharge phase with an effective rainfall of about 100 mm; second, a saturation phase, when 80% of the effective precipitation is drained mostly by runoff and hypodermic flows; third, a drying phase. Soil waterlogging events usually occur during the saturation phase. They are due to several forms of flow: surface runoff associated with return flow, hypodermic flow caused by the presence of soil layers with lower hydraulic conductivity in the subsurface (swelling clays and plowing sole) and groundwater flow with intermittent connection of the soil water table in the hillside to the alluvial groundwater table. We also conducted independent seismic refraction tomography analyses that validate localized waterlogging patterns along the catchment and open the way to spatializing areas with high waterlogging potential at the scale of the study plot.

Abbreviations: CEC, cation exchange capacity; DEM, digital elevation model; ETR, real evapotranspiration; GHG, greenhouse gases; OZCAR, Critical Zone Observatories Network; P, precipitations; WRB, World Reference Base for Soil Resources; XRD, X-ray diffraction.

This is an open access article under the terms of the [Creative Commons Attribution](https://creativecommons.org/licenses/by/4.0/) License, which permits use, distribution and reproduction in any medium, provided the original work is properly cited.

© 2023 The Authors. *Vadose Zone Journal* published by Wiley Periodicals LLC on behalf of Soil Science Society of America.

1 | INTRODUCTION

Waterlogging alters the functioning of the soil ecosystem. Indeed, the anoxic conditions that develop in a durably waterlogged soil have an impact on greenhouse gases (GHGs) production and emission. N₂O emissions, which represent 42% of all GHGs emitted by the agricultural sector in France (CITEPA, 2020), are increased by denitrification processes (Hu et al., 2010; Wang et al., 2020). Moreover, crop yields are reduced by these anoxic conditions, and water saturation of the soil pore space leads to soil compaction (Grimaldi & Tessier, 1986) and makes access to the plot difficult for the farmer (Guiesse & Bourgeat, 1991). Many factors contribute to soil waterlogging. In soils with poor internal drainage and no topographic gradient, such as Luvisols, water infiltrates vertically until it encounters an impermeable layer, creating a perched water table and waterlogging. This phenomenon has been widely documented, particularly in the context of pipe drainage networks, in the Netherlands (Bouma, 1981; van Lanen et al., 1992), in the alluvial terraces of the Garonne River in southwestern France (Bernot, 1961; Bouzigues & Vinas, 1989; Bouzigues et al., 1998; Concaret, 1981; Favrot et al., 1992; Guiesse & Bourgeat, 1991; Michel & Tessier, 2003; Tessier et al., 1992; Zimmer et al., 1991) or in Germany (Salvador et al., 2011; Hartmann et al., 2012). Waterlogging also occurs downslope of watercourses due to rising groundwater levels, which can cause more or less permanent waterlogging depending on groundwater fluctuations (Legros, 2007). Other studies have focused on cropping practices that disturb the soil structure and enhance runoff due to an impermeable sublayer, like in the Czech Republic (Kodešová et al., 2011), Burkina Faso (Spaan et al., 2005), South Africa (Podwojewski et al., 2011), or Southeast Asia (Janeau et al., 2014; Valentin et al., 2008). Waterlogging may also occur as a consequence of topographic gradient, where an area of depression area in the end of a slope causes water to accumulate from runoff and hypodermic flow. In addition to topographic waterlogging, water accumulation in molassic hills also results from water flow converging in a permeable level due to substratum heterogeneity, such as sand lenses (SLs), as reported by Revel (1982), Concaret (1981), Paegelow et al. (1991).

Molassic formations are present in many regions of the world (Amanieu et al., 1984; Hoorn et al., 1995; Jacquin et al., 1992; Shalaby et al., 2006; Smith et al., 1980) and are used for intensive agriculture in southwestern France. Yet, the specific flow patterns causing waterlogging in the clayey–calcareous soils developed in molassic formations are poorly documented.

The term molassic formation refers to continental deposits such as conglomerates, sandstones, and shales or marls eroded from mountains and deposited in rivers and lakes. Moreover, clayey calcisols in molassic hills share specific properties with soils developed around the Mediterranean basin, due to high

Core Ideas

- An interdisciplinary approach (pedology, hydrology, and geophysics) highlights flow paths in hilly calcisols.
- Seismic geophysics reveals heterogeneities of the molasse material that drives intermittent downslope connectivity.
- Soil porosity value around 100 mm both corresponds to the soils water adsorption and water supply capacities.
- The sand lens acts like a local captive aquifer for a period of 4 months starting in winter.

calcium carbonate and clay contents (Cerdà, 1996; Ruellan, 1984; Sandler, 2013; Terefe et al., 2008). These soils are subject to profile rejuvenation by erosion on steep slopes as found in other watersheds such as Cap Bon in Tunisia (Lagacherie et al., 2013; Mekki et al., 2018). Deep in these soils, precipitated calcareous concretions often result from waterlogging episodes (Bouzigues et al., 1997; Tassinari et al., 2002). The purpose of the present study is to gain a better understanding of the characteristics and hydric functioning of these soils, in order to optimize their agronomic potential and ecosystem services, such as GHG emissions.

Molassic formations are often marked by a morphogenic landscape with numerous landslides (Calvet et al., 2021). In the Pyrenees, a thick marly sedimentary layer accumulated from the last Eocene-Miocene orogenic period until the beginning of the Pliocene (Canérot, 2008). This results in a heterogeneous sedimentary formation with an average thickness of 330 m (Calvet et al., 2021) widely observed in all interfluves of southwestern France (Hubschman, 1975). The clayey and calcareous composition of these sediments results in an overall low hydraulic conductivity around 10⁻⁹ m/s, like in similar facies sedimentary deposits, such as the Toarcian marls (Lucas & Vaute, 2011). Such a low hydraulic conductivity promoted waterlogging and hydric erosion, predominantly during the successive Quaternary glaciations (Meyer & Guillet, 1980; Revel & Bourgeat, 1981). Since the Middle Ages, tillage increases erosion in these hillside landscapes (Guiesse & Revel, 1995; Revel et al., 1989), as it induces a thinning of the soil from the summit and a thickening of the soil profiles at the bottom of the slope. Tillage-induced erosion has also been described in other Mediterranean regions (Alías et al., 1997; Quijano et al., 2020). Soil distribution in the toposequence may be disrupted by tillage, as documented by Revel (1982). Moreover, soil scientists have described this soil cover as a highly heterogeneous mozaic (Revel & Guiesse, 1995).

On most soils of the molassic formations in southwestern France, including the study area, cereals and oilseeds are grown intensively. Environmental pressures, such as nitrogen inputs and tillage, contribute to the degradation of water quality (Ponnou-Delaffon et al., 2020). The alteration and contamination of soils (Bur, 2008; Redon et al., 2013; Gandois et al., 2011; Perrin et al., 2008) and sediments (Chaumet et al., 2021; Wu et al., 2021) resulting from soil erosion, as well as the processes involved in contaminant transfer (nitrogen, metals, pesticides), notably during flood events, have been investigated intensively at the catchment scale (Taghavi et al., 2010; Roussiez et al., 2013). In 2020, Ponnou-Delaffon et al. (2020) highlighted the predominance of runoff and subsurface flow during flood events. However, in these studies, the physical properties of the soils have often been neglected due to their high variability, except in Ferrant et al. (2016) where the available water capacity is spatialized by model inversion, based on satellite observation.

The purpose of the present article is to identify water pathways in molassic hills and locate biogeochemical hotspots where GHGs are potentially most intense. The aim is also to specify the physicochemical mechanisms that shed light on the hydrodynamic properties of the soils and their potential for waterlogging.

For this purpose, we combined several approaches such as pedological, hydrological, and geophysical characterizations. Several soil surveys and analyses were carried out at key locations in an agricultural area. Soil saturation and soil water potential were monitored with piezometric and tensiometric time-series measurements, as well as hydrological monitoring at the outlet of the watershed. Finally, geophysical measurements using seismic refraction tomography aimed to relate the observed flow patterns to topography and soil properties. Although the parent material is highly heterogeneous, the geomorphology of these molassic hills is marked by a repeated steep slope. The tops of the ridges are often large convex surfaces, erosion is active, and the soils are shallow, calcareous, like the parent material. Farmers used to protect soils with embankments to mitigate the slope. In the middle of the slope, moisture stains frequently disturb the crops. At the bottom of the slopes, materials accumulate along the rivers, resulting in deep colluvial soils. These are the three types of geomorphological sites we have chosen for our observations.

2 | MATERIALS AND METHODS

2.1 | Study site

Our study site is the Montoussé experimental catchment area located in the municipality of Auradé, 30 km west of Toulouse, in southwestern France. The watershed covers an area of 328 ha of which 88.5% is cultivated (Perrin et al., 2008). The elevation varies from 172 to 273 m above sea level.

The average slope is 9% but locally exceeds 25%. The soils of the catchment are mostly Calcaric Cambisol and Colluvic Fluvisol with more or less stagnic and gleyic properties. They developed in the molassic sedimentary deposit of the Burdigalian and Helvetian periods of Miocene (Bur, 2008; Perrin et al., 2008). The site has been monitored since 1985 and has been the subject of numerous studies. Several monitoring devices are located in the catchment area, notably at the catchment outlet. These devices enable the investigation of the transfer of contaminants and of natural dissolved and suspended matters in the environment, as well as the role of flood events and farming practices on weathering processes and exported fluxes (see Perrin et al., 2008 or Ponnou-Delaffon et al., 2020 for details). A modeling approach was performed to assess the risk of pesticides and nitrogen transfer to surface waters (Macary et al., 2013) as well as to evaluate the influence of different land use scenarios (Ferrant et al., 2011; Casal et al., 2019). This experimental catchment area (<http://bvea.sedoo.fr>) belongs to the Critical Zone Observatories Network (OZCAR) (Gaillardet et al., 2018).

The present study focuses on two adjacent cultivated plots located close to the outlet (43.55897, 1.064341 in WGS 84) (Figure 1). We selected these plots because of their geomorphological characteristics, and because of the presence of points of interest that allow investigation of the hydrological functioning of the catchment at the local intra-plot scale. Previous works (Bur, 2008; Perrin et al., 2008; Ponnou-Delaffon et al., 2020) showed that these plots' pedological features are representative of all the catchment. Both plots have the same crop rotation, which is the representative of the area: wheat/sunflower/wheat. Faba bean intercropping has been introduced in 2019 between wheat and sunflower. From April 2020 to July 2021; sunflower was grown, followed by wheat. During this period, hydric parameters have been monitored from September 2020 to September 2021 to stick to the hydrological year.

2.2 | Location and protocol for soil sampling

Using an auger, we collected samples from the two adjacent plots (Figure 1). A first set of samples was collected from plot 1 (bounded by the continuous line, Figure 1), along the NE–SW axis parallel to the slope (points A–E), from the surface to a depth of 70 cm. These samples were used to study the soil textural variations along the toposequence and the clay fraction mineralogy.

In plot 2 (bounded by the dotted box, Figure 1), three soil samples were collected at a greater depth to investigate the whole soil profile. These samples, named RS for “riverside,” SL for “sand lens,” and EM for “embankment,” were selected because of their different topographic positions and contrasting hydrological functioning. The RS point is located at the bottom (183 m elevation) of the plot along the stream in a low

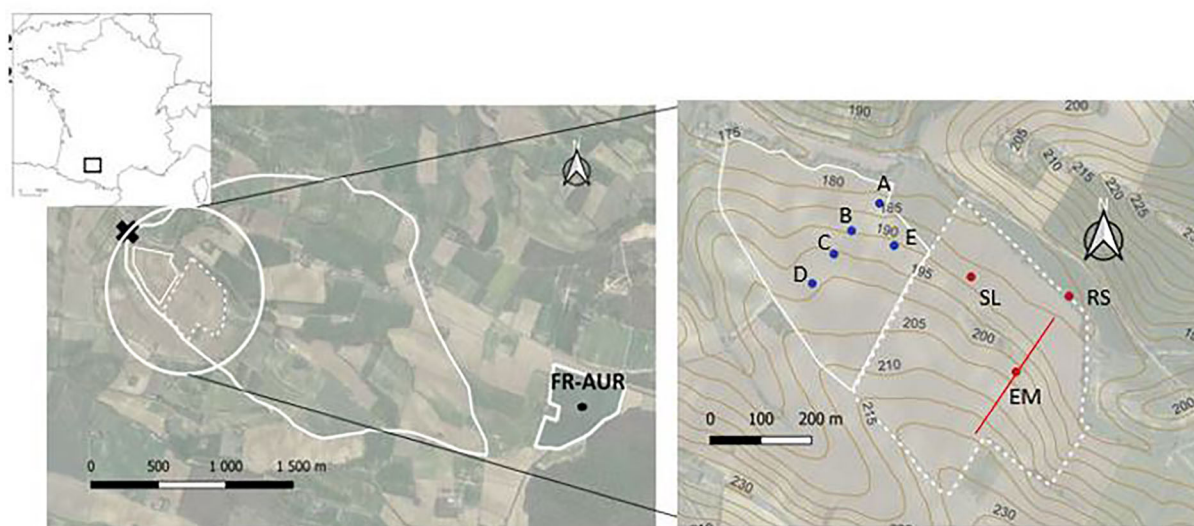


FIGURE 1 Study plots inside the watershed. (X: outlet of the watershed, **FR-AUR**: meteorological station; A–E: toposequence points; RS, riverside; SL, sand lens; EM, embankment. The redline indicates the position of the geophysical transect). Plot 1: continuous white line, plot 2: dotted white line. The contour lines are spaced 5 m apart.

slope area. The soil is deep there and was investigated down to 220 cm. The SL point is in a flat, often waterlogged area (188 m elevation). The SL profile was investigated down to 130 cm. The EM point (202 m elevation) is located at mid-slope above an embankment of ancient anthropogenic origin. The EM profile was investigated down to 140 cm. The three piezometer holes were dug down to the bottom of the three profiles, in order to record water fluctuation in the soil profiles. Points SL and EM are located on the plot cultivated with sunflower from April to September 2020 and then wheat from November 2020 to July 2021, whereas RS is located on the edge of the watercourse, in the grass strip which does not receive any fertilization and where the soil has not been tilled since 1992.

2.3 | Soil analyses

Prior to analyses, the soil samples were air-dried and sieved to 2 mm. Particle size distribution in five fractions (clays $<2\ \mu\text{m}$, fine silts (2–20 μm), coarse silts (20–50 μm), fine sands (50–200 μm), and coarse sands (200–2000 μm)) was determined by the Robinson pipette method according to the standard protocol NF X 31-107. As these soils have carbonated horizons, granulometric analyses were carried out with or without prior decarbonation. The cation exchange capacity (CEC) was determined by the cobaltihexamine method (Ciesielski et al., 1997), which is best suitable for calcareous soil according to the NF X 31-130 standard. CaCO_3 content was determined by elementary analysis according to the NF ISO 10694/NF ISO 13878 standard (<https://chemicalanalysis.cnrs.fr>).

The clay fraction mineralogy, which impacts the hydraulic conductivity of soils (Benson & Trast, 1995; Pusch, 2006), was determined by X-ray diffraction (XRD). Sample preparation included (i) decarbonation with acetic acid and sodium acetate buffer at pH 5, (ii) destruction of organic matter with 5% H_2O_2 v/v at 40°C (NFX 31-107), (iii) dispersion in a solution of a 1 mol/L of NaCl and lastly extraction of the $<2\ \mu\text{m}$ fraction by sedimentation. Aliquots of the $<2\ \mu\text{m}$ fraction were saturated with calcium (CaCl_2 0.5 mol/L) and then washed to remove excess salts. Oriented preparations were obtained by depositing the clay suspensions on glass slides and drying them at room temperature (air dried: AD). The slides were also solvated with ethylene glycol (EG) vapor at 50°C in a desiccator for 16 h. XRD patterns of the oriented preparations were recorded on a Bruker D8 Advance diffractometer ($\text{Cu}\ K_\alpha$ radiation) from 2.5 to 35° 2θ . The XRD patterns were decomposed in the 2:1 clay mineral range (3°–14° 2θ) using the procedure described by Lanson (1997). Background subtraction was performed using the Fityk 0.8.2 peak fitting software (Wojdyr, 2007), and introducing the minimum number of curves to obtain the most realistic mineral composition. The different peaks obtained during the decomposition were attributed to clay mineral species according to Moore and Reynolds (1997), Righi et al. (1995), and Velde (2001). Decomposition of the diffractograms (Hubert et al., 2009; Caner & Hubert, 2012) allowed us to estimate relative peak intensities of each 2:1 clay mineral and thus to compare the 2:1 clay mineral assemblage of the different soil horizons. Variations in relative intensities correspond to variations in mineral quantities as soils develop from the same parent material (Lanson, 1997).

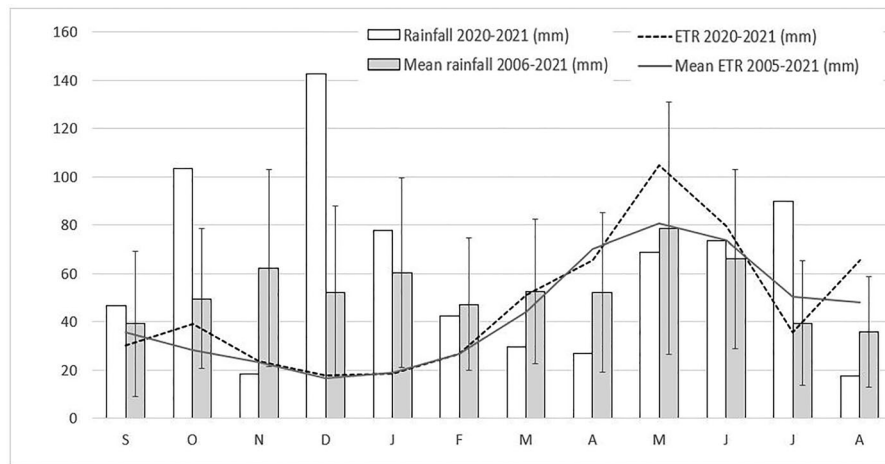


FIGURE 2 Monthly rainfall with standard deviation and real evapotranspiration on the Montoussé catchment.

2.4 | Monitoring of soil water level and potential, climate, and hydrology

Soil water table levels at the RS, SL, and EM points were recorded over a full year from September 2020 to September 2021 (10-min time step), by piezometers equipped with Level TROLL water level probes, at depths of 220, 130, and 140 cm, respectively. Water levels in the piezometers are always expressed in relative elevation, as compared to the respective soil surface levels. In order to monitor the soil hydric potential of the unsaturated soil, from November 19, the SL site was also equipped with a set of watermark tensiometers (three tensiometers at 30 cm and three others at 60 cm; hourly time step).

Rainfall data were collected at the watershed station. Real evapotranspiration (ETR) was calculated thanks to the Eddy-covariance flux tower located at the FR-AUR site (Figure 1), close to the catchment area monitored within the framework of the ICOS network (Tallec et al., 2013). The mean annual precipitation (P) is 635 mm/year. Monthly rainfall distribution (Figure 2) is the representative of a degraded oceanic climate, with a wet period with low ETR (0.5–1 mm/day) from October to February, and a dry period with high ETR (2–3 mm/day) from April to September. Aggregated on a daily basis, P-ETR enables the estimation of effective precipitation, which drives soil recharge and water flow formation. Rainfall amount in 2020–2021 was representative of the average past climate (2006–2021), except for October and December, which showed an excess of 90 mm; March and April, which showed a deficit of 40 mm; and July, which showed an excess of 50 mm rainfall (Figure 2).

The stream water level at the watershed outlet is measured by a water level gauge with an hourly time step and converted into flow by a regularly readjusted gauging curve (see Ponnou-Delaffon et al., 2020 for details). The stream specific water discharge, in mm/h, is determined by dividing these water flows by the surface area of the catchment.

2.5 | Near surface geophysics methodology

Geophysical measurements were used to identify areas of similar signals and to relate them to pedological, topographical, and morphological properties. We aimed at determining factors predisposing to waterlogging, at the plot level, with a view to extrapolating to a larger scale. We performed seismic refraction tomography using the pyGimli library (Rücker et al., 2017) to estimate pressure-wave velocities (V_p) on a transect between points EM and RS on October 7, 2019 (Figure 1). We could thus image the subsurface structure and detect competent zones at depth. Multichannel analysis of surface waves was also carried out using the SWIP library (Pasquet & Bodet, 2017) to estimate shear-wave velocities (V_s). Using both V_p and V_s velocities, we were then able to calculate the Poisson ratio (the so-called ν) (Equation 1), an indicator of the soil, and parent material moisture at the time of the measurement (Pasquet et al., 2015):

$$\nu = \frac{1}{2} \times \frac{\left(\frac{V_p}{V_s}\right)^2 - 2}{\left(\frac{V_p}{V_s}\right)^2 - 1} \quad (1)$$

Seismic refraction tomography thus allowed us to estimate the depth of the saturated level for this EM-RS transect and its evolution as a function of the topography. This provided complementary data for the elucidation of flow patterns.

3 | RESULTS

3.1 | Pedologic features

Although the three topsoils are very close in terms of their granulometric composition (Figure 3), the SL profile is the most clayey one with ~45% clay fraction in the A and Bkg

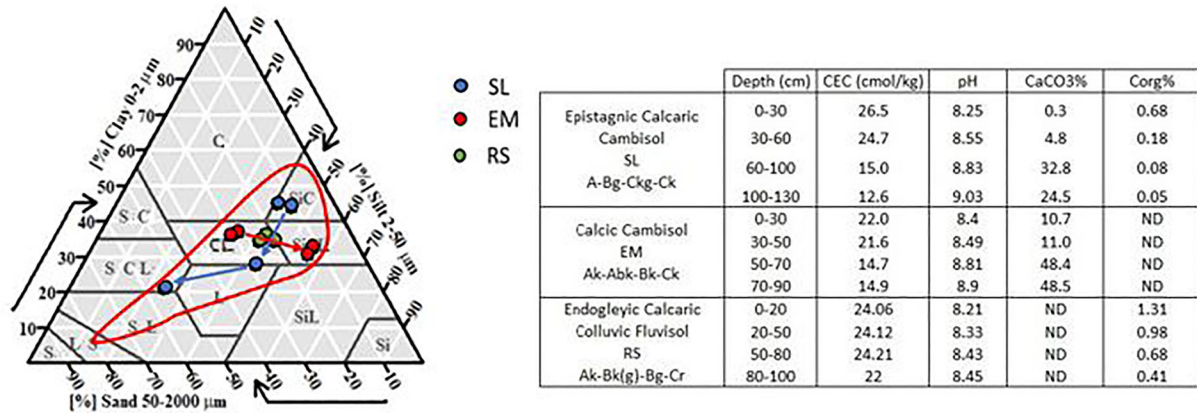


FIGURE 3 Granulometric evolution along soil profiles (USDA) with the associated table of cation exchange capacity (CEC), CaCO₃, and pH evolution. Arrows indicate texture evolution down the soil profiles. The red triangle is the area of textural evolution in other soil profiles studied in the same watershed (Bur, 2008). EM, embankment; RS, riverside; SL, sand lens.

horizons (IUSS Working Group WRB, 2022). In terms of texture, the SL profile lies between silty clay (SiC) and Clay textures. In the subsoil of the SL profile, a significant decrease in the clay fraction from 45% to 22% is accompanied by an increase in the sand fraction from 15% to 55% (mainly fine sand). The texture of the SL profile then evolves from SiC to clay loam/loam in Ckg horizon to sandy clay loam in the Ck horizon below 100 cm depth. In these two deep horizons, the percentage of silts decreases sharply from 45 to 25, in favor of sands, which increase from 30 to 55. The majority (60%) of these granulometric sands are fine sands not affected by decarbonation. The remaining 40% are coarse sands affected by decarbonation. The CaCO₃ content increases from 0.3% in the topsoil to 25%–30% in the subsoil. The carbonate content is mainly present in the fine silt fraction and in the coarse sand fraction. The redoximorphic features start at 35 cm depth with Fe and Mn concretions and mottling revealing epistagnic conditions in the Bg horizon. Deeper, the redoximorphic feature becomes obvious with sharp CaCO₃ concretions (>10%) in the Ckg horizon. In the sandy Ck sublayer, the mottles disappear in favor of a Fe-poor horizon. In total, according to the IUSS Working Group WRB (2022), this SL profile is characteristic of an Epistagnic Calcaric Cambisol with this layer sequence: A–Bg–Ckg–Ck.

The EM profile (Figure 3) exhibits a CL texture for the first 50 cm (Ak and ABk horizons). Deeper, in the Bk horizon, the silt fraction sharply increases from 35% to 55%, whereas the sands decrease from 30% to 10%, resulting in a shift to the SiC loam texture. Below 70 cm depth, the Ck horizon exhibits a uniform pale-yellow color without redoximorphic features. Below 50 cm depth, 85% of the silty fraction is composed of fine silts. The soil at the EM point is the most carbonated of all three investigated points: The CaCO₃ content increases from 10% in the topsoil to 50% at a depth of 50 cm. In the Bk horizon, scarce redoximorphic features (<5%) reveal some gentle stagnic conditions. In total, the EM profile is characteristic of a Calcaric Cambisol with this layer sequence: Ak–ABk–Bk–Ck

The evolution of pH with soil depth follows that of CaCO₃ for both profiles with pH ranging from 8.25–8.4 in the topsoil to 8.9–9.0 in the subsoil (Figure 3).

Below 50 cm depth, the fine silt and coarse sand fraction strongly decrease after decarbonation, indicating that carbonates are mainly present in these fractions.

At the RS point, the soil is deeper (>220 cm) and more homogeneous than at the EM and SL points, with a CL texture extending over 100 cm from the Ak horizon to the subsoil Bkg horizon. The CEC and pH values also remain stable throughout the soil profile down to the Cr horizon and are close to the values measured in the topsoil of the other profiles (Figure 3). The CaCO₃ content decreases with depth for this profile, indicating a colluviation with a continuous uphill contribution. Moreover, the vicinity of the stream favors long-lasting water-logging, leading successively to soft redoximorphic features in the Bk(g) horizon, strong redoximorphic features in the Bkg horizon, and a gleyic Cr horizon at 120 cm depth. In total, the RS profile is characteristic of an Endogleyic Calcaric Colluvic Fluvisol with this layer sequence: Ak–Bk(g)–Bkg–Cr.

3.2 | Clay fraction mineralogy

The clay fraction mineralogy determination was performed on the A–E transect, and at the SL and EM points. Here, only the results for the SL profile are presented, displaying a strong mineralogical evolution from surface to depth. However, similar results were obtained with the other points. The main clay minerals identified in the <2 μm fractions using XRD are smectite (15 Å AD; 17, 8.5 Å EG), chlorite (14.2, 7.1, 4.72, 3.54 Å), illite (10.0, 5.0, 3.33 Å), and kaolinite (7.15, 3.57 Å) and illite/smectite interlayered minerals (10–15 Å AD; 10–17 Å EG) (Figure 4). Kaolinite and chlorite are the least abundant clay minerals in the overall signal. The decomposition of the XRDs patterns in the angular range 3°–14°2θ (Figure 5) shows a dominant contribution of

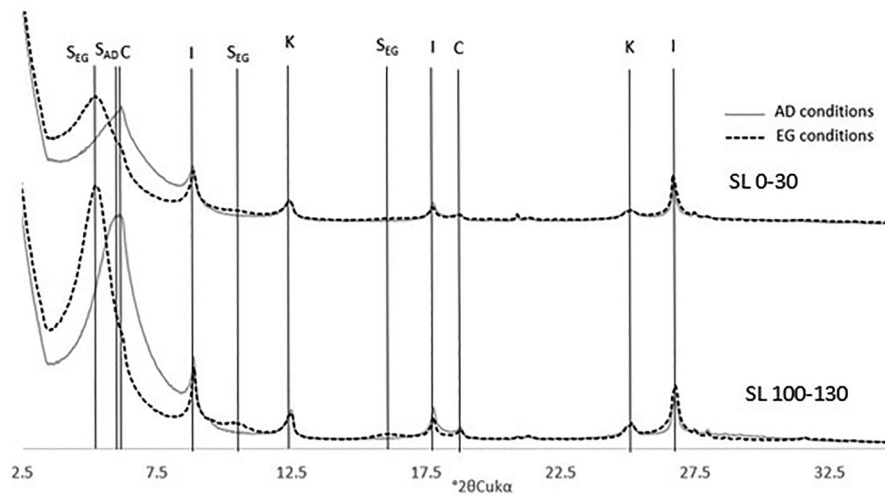


FIGURE 4 Diffractograms of the clay fraction with peaks characteristic of clay minerals for sand lens (SL) point at 30 and 130 cm depth. S, smectite; C, chlorite; I, illite; K, kaolinite

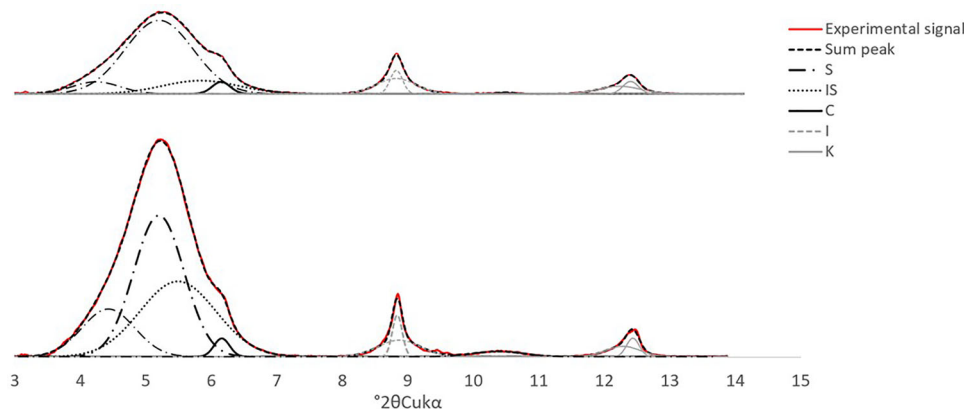


FIGURE 5 Decomposition of X-ray diffraction (XRD) patterns for sand lens (SL) samples in ethylene glycol (EG) treatments. S, smectite; IS, mixed interlayered minerals; C, chlorite; I, illite; K, kaolinite

smectites and illite/smectite mixed layers in the diffraction signal (70%–80%).

The deeper into the soil of the profiles, the stronger the expandable minerals signal, notably for SL (+10%) as shown in Figures 4 and 5, indicating an increase in their proportions. Figure 5 also shows (i) that swelling clay minerals are the dominant minerals of the clay fraction and (ii) that the contribution of smectites to the diffracted intensity decreased from 70% at soil surface to 55% at 100 cm, whereas that of illite/smectite mixed layers increased from 10% to 35%. The proportion of the signal attributed to chlorite and kaolinite does not change significantly. The part of the signal attributed to illite decreases from 10% in SL 0–30 cm to 5% in SL 100–130 cm samples.

The profiles from the toposéquence A–E (Figure 1) show similar textural classes (clay loam), with little evolution in the first 50 cm and with a similar clay mineralogy. The contri-

bution of the different clay minerals is similar to that of SL profile samples (Figures 4 and 5).

3.3 | Hydrological monitoring

Based on the cumulative stream water discharge and the cumulative effective rainfall, the hydrological year shows a three-phase pattern (Figure 6). The first phase runs from September to mid-December 2020, with a cumulative effective rainfall (P-ETR) of 103 mm and a cumulative drained water height of 23 mm, that is, only 22% of the rainfall input. The resulting increase in soil moisture corresponds to the soil recharge phase. The mesoporosity must first be filled in order to reach the drainage phase. The saturation phase runs from mid-December 2020 to late March-beginning of April 2021. During this period, the cumulated effective rainfall is 164 mm,

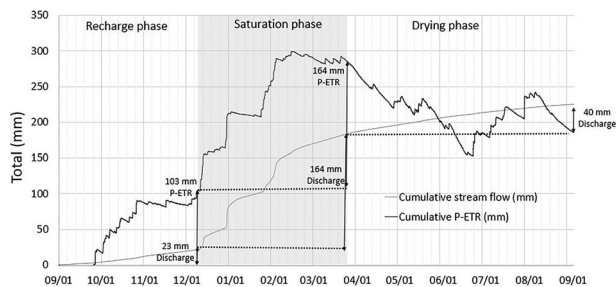


FIGURE 6 Cumulative stream discharge versus cumulative P-real evapotranspiration (ETR), from September 2020 to September 2021. Phase I runs from September 22 to December 10, 2020. Phase II runs from December 11, 2020 to March 31, 2021. Phase III runs from April 1 to September 30, 2021. Arrows indicate the cumulative rainfall and flow for each phase.

and a drained water height of 164 mm is observed, that is, 100% of the input. It may be assumed that the soil mesoporosity is saturated, and that most of the rainfall is drained to the watercourse, owing to active macroporosity. The third phase, the soil-drying phase (Figure 6), runs from the end of March 2021 until September 2021. Until the end of June, ETR exceeds precipitation. The P-ETR then becomes negative; the cumulative decrease reflects a water deficit. The emptying mesoporosity supplies water for evapotranspiration, for a total of 113 mm from March 31 to June 20 (Figure 6). Thereafter, heavy summer rainfall results in a positive P-ETR, contributing to the total drained water height, which achieves about 40 mm for the entire drying phase.

In order to address climate variability, we studied 12 years from 2006 to 2018 (data not shown). We monitored the effective rainfall versus the outlet stream flow. Obviously, rainfall shows a strong interannual heterogeneity. Total annual stream discharge exceeds 200 mm in the wettest years, whereas it is less than 100 mm in the driest years. Still, we found that the three-phase hydrological year pattern recurs every year, from 2006 to 2018. In order to better visualize these three successive phases, we selected three typical years, a dry year (2010–2011), an average year (2006–2007), and a wet year (2020–2021), to display in Figure 7 the cumulative flows as a function of the cumulative effective rainfall, from September 1 (year n) to August 31 (year $n + 1$). For each year, the slopes of the curves differ significantly over three periods, reflecting an evolution of “yield of flow” (Yield Q) varying throughout the hydrological year between day d and day $d + n$:

$$\text{Yield}Q_d^{d+n} = \frac{\sum_d^{d+n} (Q_{\text{outlet}})}{\sum_d^{d+n} (P - ETR)} \quad (2)$$

The slope breaks of the curves in Figures 6 and 7, along with the chronicles of rainfall and flow, led us to divide each hydrological year into three successive periods.

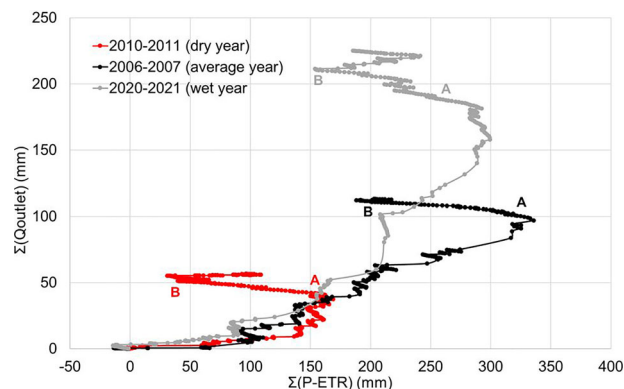


FIGURE 7 Cumulative flows at the outlet as a function of cumulative P-real evapotranspiration (ETR) from 09/01 to 08/31, for three typical hydrological years: 2010–2011 (dry year), 2006–2007 (average year), and 2020–2021 (wet year). “A” and “B” delimit the hydric deficit.

A first recharge phase always occurs in autumn with a very low Yield Q (low slope, on average 0.14 ± 0.09). The median rainfall excess for the recharge phase (98 ± 29 mm) is very close to that of the 2020–2021 hydrological year. A break then occurs between November and January when the Yield Q suddenly rises toward 1 (Figure 7). During this second phase, the saturation phase, the drained water discharge can be very high (>150 mm), as in 2020–2021, whereas it remains below 50 mm for the driest years, as in 2010–2011. The transition to the third phase, the drying phase, is clearly visible for the three typical years represented in Figure 7 (A points). High spring temperatures increase crop water uptake (Figure 2), leading to water deficits (negative P-ETR), and thus a gradual decrease in $\Sigma(P-ETR)$ between points A and B in Figure 7. During the drying phase, without any excess rainfall, the flows return to very low values. At that moment, the stream flow is sustained by groundwater; we can therefore neglect soil drainage and thus simplify the hydric balance. Consequently, the entire water deficit is equivalent to the decrease of the soil water stock, as we considered that during the recharge phase, all the rainfall excess contributes to the recharge of the soil water stock. Finally, the change in soil water stock (ΔS) between two dates d and $d + n$ is given by the following equation:

$$\Delta S = \sum_d^{d+n} (P - ETR) \quad (3)$$

In autumn, (P-ETR) is positive, and the soil water stock increases. Conversely, in spring–summer, water deficit occurs over more or less long periods, during which the soil water stock decreases as a result of crop uptake. Thus, actual evapotranspiration is driven by the soil available water. The water supplied by the soil was thus calculated using Equation (3), over the periods of water deficit delineated by points A and B in Figure 7, for each hydrological year, except for 3 years.

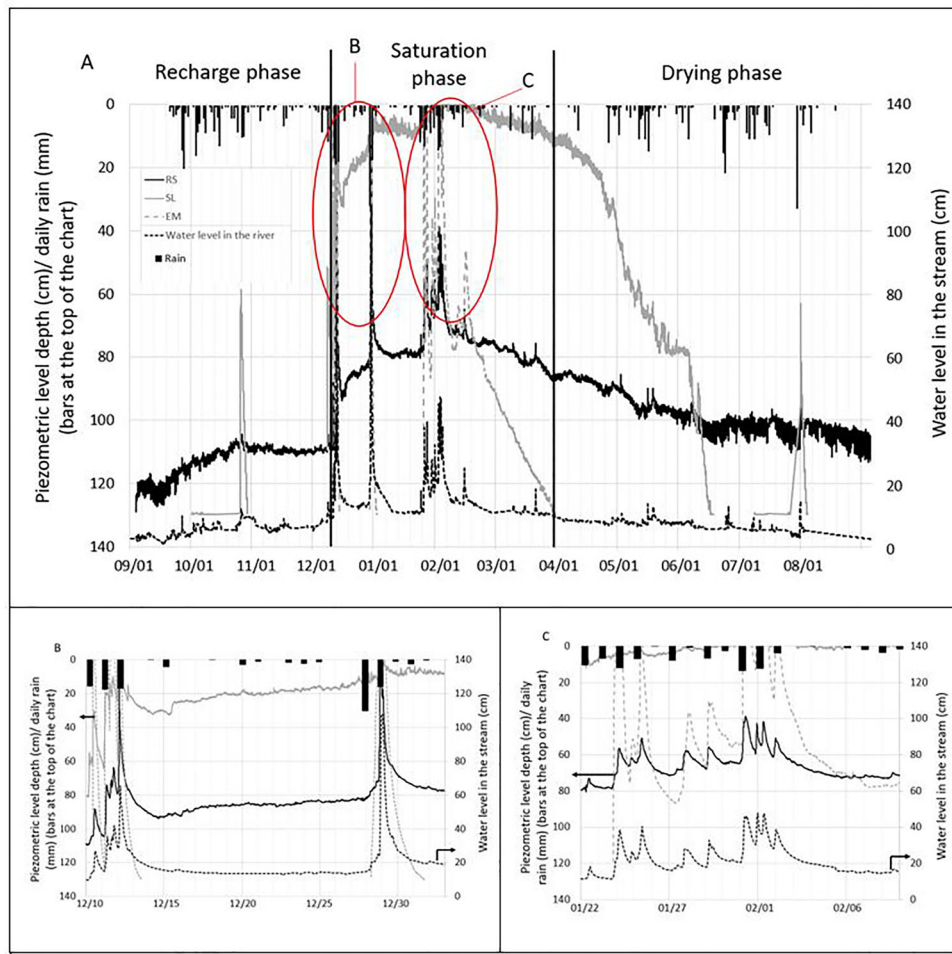


FIGURE 8 Piezometric patterns (2020–2021) at riverside (RS) (black), sand lens (SL) (gray), and embankment (EM) (dotted gray) points, compared to the water level in the stream at the outlet (dotted black) throughout the investigated period (A) from September 1, 2020, to September 1, 2021, a focus (B) on the beginning of the saturation phase, from December 10, 2020, to January 02, 2021, and a focus (C) on the core of the saturation period from January 22, 2021, to February 09, 2021. Primary axis: piezometric level (cm) and daily rain (mm, bars at the top of the chart). Secondary axis: water level in the stream (cm).

Indeed, for 2007–2008, 2009–2010, and 2016–2017, precipitation was distributed throughout the year, and no dry period was long enough to allow the calculation. On average, we obtain 104 ± 37 mm.

Ultimately, we conclude that the amount of water stored in the soil in autumn is of the same order of magnitude as the amount of soil water desorbed for summer evapotranspiration, around 100 mm.

3.4 | Piezometric and tensiometric monitoring

Unlike the previous hydrological analysis for which we had a large set of past data, piezometric and tensiometric measurements have only been carried out since September 2020. For readability, we will only present here the 2020–2021 measurements that are consistent with those of 2021–2022.

The piezometric records in Figure 8 show different water regimes at each of the measurement points. Despite significant altitude differences among the three points (14 m from EM to SL and 5 m from SL to RS), the three water levels differ by only a few decimeters. Although the water level at RS evolves between 0 and 120 cm depth all over the year, at SL, it was visible at such depth only during the saturation phase, and only for 2 months at EM.

Thus, during the recharge phase from September to mid-December 2020, only the RS piezometer is in water (Figure 8A) with a water level around 110 ± 2 cm depth. The SL piezometer shows a transient water level rise on 10/31/2020 correlated to the heavy rainfall event of 10/25/2020 (Figure 8A). Then, the water level in the piezometer falls below the sensor level (130 cm) within 2.5 days, whereas the height of the stream at the outlet does not show any significant variation. The water level in the EM piezometer remains below the sensor (140 cm) over this period.

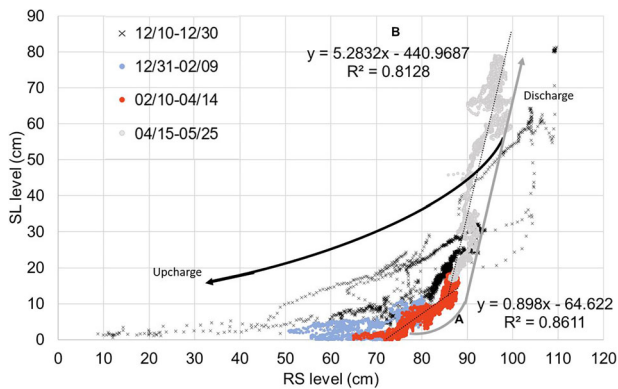


FIGURE 9 Relationship between sand lens (SL) and riverside (RS) piezometric levels during the saturation and discharge phases of the SL piezometer, from December 10, 2020 to May 25, 2021. Linear regressions: evolution of the piezometric level during discharge between (A) 75 and 85 cm depth, and (B) deeper than 85 cm.

From the beginning of December 2020 until the end of March 2021, during the saturation phase, the three points show different trends in their water level evolution (Figure 8A–C). Water level rises are sporadic at the EM point until the end of January, whereas they are continuously observed at RS and SL. The rise in the piezometric level of the alluvial water table (RS) correlates closely with the rise in the level of the water table in the hillside (SL point) between the floods of December 10 and 28. Throughout the winter period, the RS piezometer records significant rises concomitant with the floods recorded at the outlet. More specifically, during the saturation phase, the water levels measured at the outlet and by the RS piezometer are quite similar and simultaneous (Figure 8B). The strong synchrony between the water level in the stream and the alluvial groundwater (RS) indicates that the alluvial groundwater is connected to the stream water discharge.

The water table level in the slope (SL point) rises sharply following the heavy rainfall of December 7 (+50 cm) and December 10–12 (+70 cm). Then the level drops (–20 cm after each rise, Figure 8B) which seems to indicate that the water supply is essentially lateral and superficial at this stage. From December 15 until the end of February, the water table at the SL point remained at a high level (0 to –20 cm depth), even without rainfall, suggesting that the water supply is sustained by underground flows of deeper and perennial origin. This statement is supported by the relationship between SL and RS piezometric levels (Figure 9). As soon as the piezometric level of RS becomes deeper than 85 cm, the SL water level evolves rapidly either in upcharge phase (Figure 9, black cross) or in discharge phase (Figure 9, light gray points), with a ratio of 5.3:1 (Figure 8B) in piezometric evolution between RS and SL. Figure 9 underlines a hysteresis between both phases. We assume that during the upcharge phase, groundwater flows gradually connect to the SL. A minimum depth

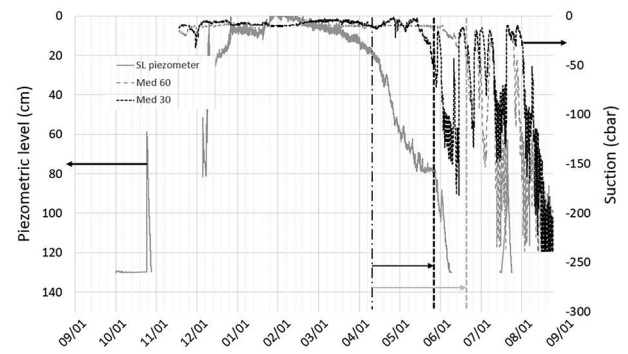


FIGURE 10 Suction head monitoring (Med 30 and 60, median values at 30 and 60 cm, respectively) of the sand lens (SL) point versus the piezometric level during a complete hydrological cycle. The black and gray arrows on the dotted vertical lines show the temporal shift between the lowering of the piezometric level and the drop in suction.

of 85 cm RS is required for RS and SL levels to remain connected. From 85 to 75 cm depth, the evolution of RS level is close to that of SL (0.9:1 ratio, Figure 9A, red points), until the profile reaches saturation. As soon as the RS piezometric level is less than 75 cm deep, the SL level remains nearly constant, very close to the soil surface (0–10 cm depth), regardless of the evolution of the RS level (Figure 9 blue points): This is the heart of the saturation phase. Indeed, for 2 months (January and February), the water level at SL does not vary significantly (Figure 8A,C) because the profile remains saturated and waterlogged by this upward supply of groundwater. The water level rises even above the soil surface (from 0.1 to 3.5 cm) for 10 days (01/30/2021–02/09/2021, Figure 8C). Tensiometric monitoring at point SL (Figure 10) indicates that the soil became nearly saturated at 30 and 60 cm depth on November 19, 2020 with soil water potential values close to –10. Med 30 and 60 values remain close to 0 during the saturation phase. However, the evolutions of the piezometric and tensiometric levels in SL differ at the end of the saturation period. Indeed, the water level in SL drops down from mid-April to the end of May, whereas tensiometers indicate a saturated soil until the end of May at 30 cm depth and until the end of June at 60 cm depth. This discrepancy between the evolution of the piezometric and tensiometric levels may be related to the soil texture. High clay content and low permeability in the upper 60 cm, characteristic of a high micro and mesoporosity, retain water in the profile during wet periods and cause saturation around tensiometer probes.

The EM piezometer is also in water at the beginning of the winter period, but discontinuously. From January 24, 2021 onward (Figure 8C), the water level fluctuates between the soil surface and 80 cm depth. The synchrony between the water levels at the EM point and in the watercourse highlights a correlation throughout the winter period (Figure 8C). Continuous rainfall maintains the water level high over this period. The very rapid rise and fall of the water levels at the EM

point (over a meter in less than an hour) make it unlikely that this is caused by permanent groundwater flow. Hypodermic flow is more likely, as the piezometer tube records measurements over its entire height. The persistence of a water level in the piezometer between January and end of March 2021 (Figure 8A) reflects the persistence of subsurface flows long after the rainfall has stopped.

From the beginning of April 2021, the soil undergoes a drying phase (Figure 6). The water levels in RS and SL piezometers remain supplied with groundwater but continuously decrease. The decrease of the water level at SL is dependent to that at RS (Figure 9). First, the evolution of the water level in SL is close to that in RS with a ratio of 0.9 cm for 1 cm drop in piezometric levels, respectively, from February 23 to March 30, 2021. After March 30, the drop in the SL level is much greater than the drop in the RS level. The decreasing ratio of piezometric level in SL shifts from 0.9:1 to 5.3:1 (Figure 9), probably because the groundwater no longer feeds the SL piezometer. From April 24, and then from May onward, a sharp drop in water level is observed in the SL piezometer, resulting in complete drying on June 14, 2021 (Figure 8A). The summer months are marked by significant daily water level fluctuations at the RS point. Tensiometric monitoring (Figure 10) also reveals the drying of the soil. During June 2021, the tensiometers at 30 cm depth record more negative suction head values than the tensiometers at 60 cm. July rainfalls moisten the topsoil, which remains wetter than the subsoil throughout the summer. The minimal measurable values (< -239 cbar) occur simultaneously, at the end of August, for both sets of tensiometers (30 and 60 cm). The EM point starts to discharge from February 13, 2021. Initially fast, the drop in the water level then follows a quasi-linear evolution that extends over a month, from the end of February until the end of March 2021 (Figure 8A). After this date, the EM piezometer remains dry at 140 cm depth.

3.5 | Physical soil and subsoil properties by means of seismic prospection

On the studied transect (Figure 1), the P-wave velocity profile plotted in Figure 11A shows a gradient from surface to depth. The velocity V_p increases with the compactness of materials. Based on the empirical relationships established between bulk density and P-wave propagation velocity by Wang et al. (2019) on sandstone with weakly calcareous cement, we consider, as a first approximation, that $V_p = 700$ m/s constitutes a good indicator of the limit between the soil explorable by plant roots and the underlying alterite. This limit is between 0 cm, directly at the slope break below the EM point, where calcareous materials outcrop, and about 300 cm at the bottom of the slope, where sedimentary deposits resulting from erosion accumulate (Figure 11B,C). Compact materials ($V_p > 2000$ m/s) can

be observed near the surface ($X = 90$ m, $Z = 190$ m), above the slope break (Figure 11A 11); in the middle of the hillside (Figure 11A 12: $X = 130$, $Z = 175$), and at the bottom of the plot (Figure 11A 13) where the transition is rapid from loose deposits with low V_p (< 700 m/s) to very compact and consolidated materials with high V_p (> 2000 m/s). At the very top of the slope, highly compact areas ($V_p > 2000$ m/s) are much deeper: at a depth of over 20 m (Figure 11A,B).

Whalley et al. (2012) have established a robust relationship among V_s (shear velocity), the bulk density, and pressure potential of the traversed material. This relationship differs fundamentally from that obtained for P-waves. Indeed, the value of the Poisson ratio (ν) is closely related to the water content of the traversed material (Pasquet et al., 2015), and more specifically to the density and matrix potential of the porous medium, as reported by Solazzi et al. (2021). Based on the tightening of the isolines from $\nu = 0.43$, we took $\nu = 0.45$ as the threshold beyond which the porous matrix is saturated. The saturation level is thus estimated between 2 and 3 m depth at the bottom of the plot and follows the topographic slope ($X = [185; 210]$) (Figure 12 13). In this part of the slope, Poisson's ratio is greater than 0.45, in the topsoil, decreases quickly between 50 and 150 cm depth, and then increases again beyond this depth until it exceeds 0.45. Here, in the down part of the hill, we note a concomitance between unconsolidated materials with low V_p and environments saturated with water ($\nu > 0.45$). On the contrary, in the uphill part, on a high topographic position ($X = 20$ m, Figure 12), the isoline $\nu = 0.45$ differs from the topographic slope. The saturation level is reached at a depth of over 15 m, much deeper than in the rest of the slope (Figure 12A–C).

4 | DISCUSSION

Based on the above results, we identified three key factors that cause waterlogging in the study area, namely, soil and subsoil composition, their spatial distribution, and slope morphology. We discuss these factors below and propose a conceptual scheme of hydrological functioning (Figure 13). This diagram shows a conceptualization of water flows during the winter period, when the SL point is saturated and the water table at its highest level (water table limit).

4.1 | A soil composition that favors waterlogging

The textures presented in Figure 3 are all centered on the clay loam class, except for the deeper horizons of the SL profile, which are sandier. The 12 granulometric analyses are the representative of the soils of the catchment in which 38 samples were previously analyzed by Bur (2008).

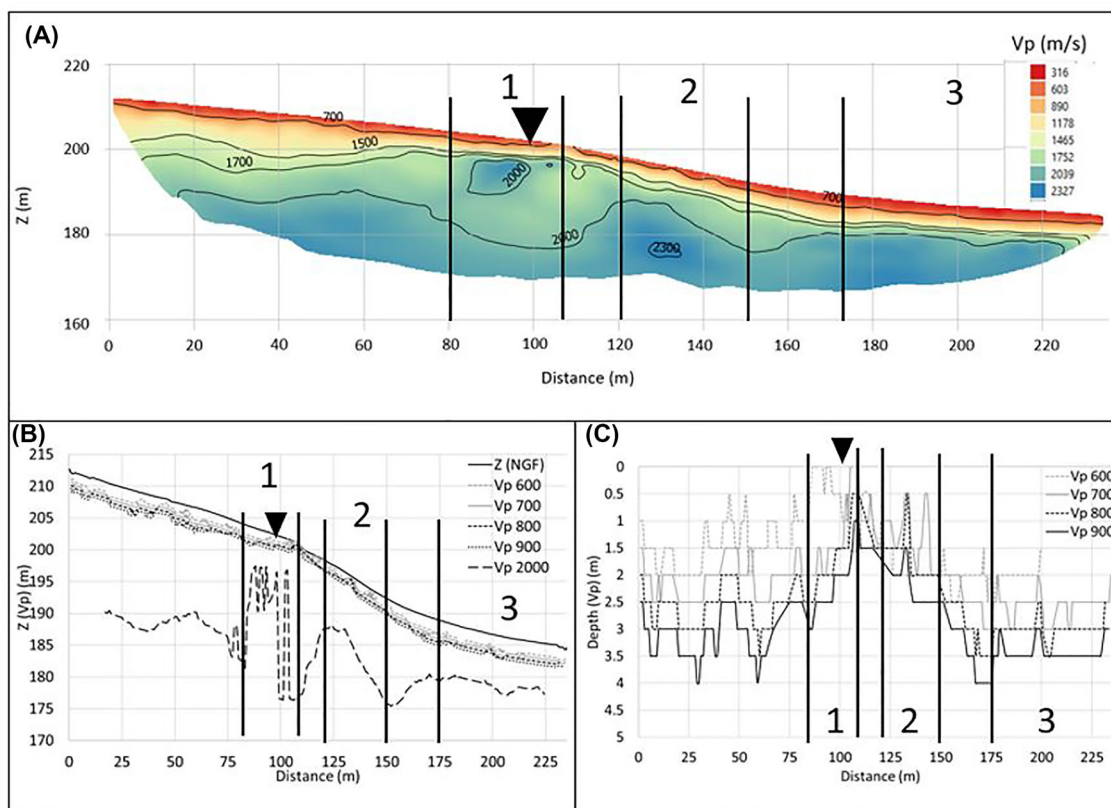


FIGURE 11 Velocity of P-waves (V_p , m/s) determined by seismic prospection along the embankment-riverside (EM-RS) transect, as a surrogate for layer compactness, versus topography (A and B) and versus depth (C) (▼: EM point, |1|: rise of compact material above EM point, |2|: rise of compact material below the EM point, |3|: increase in soil thickness with quick transition to compact material).

The surface horizon of the SL profile is decarbonated, in contrast to EM. The calcareous concretions, that are prominent at depth, are markers of an intense waterlogging of the soil, as described by Bouzigues et al. (1997) and Tassinari et al. (2002), in the Mediterranean environment. The primary carbonates present in the fine earth of the topsoil are dissolved by rainfall. A prolonged residence time of rainwater in the soil increases carbonates dissolution and leaching into the sublayers. As evidenced by our results (Figure 6), a water deficit occurs each year after a period of rain surplus. Second, evapotranspiration transfers water from the soil upward, promoting secondary precipitation of carbonates in Ckg soil horizons (photograph in Figure 13). Previous studies (Revel, 1982; Bouzigues et al., 1997; Tassinari et al., 2002) refer to these white coating around many aggregates as hydromorphic features. The textural evolution is unique within the SL soil profile, compared to the EM and RS profiles. Clay content decreases in the SL profile from surface to depth, first in favor of silt, then in favor of sand (Figure 3). The different textural evolutions with soil depth shown in Figure 3 have an impact on the hydrological functioning of the soils. Some points in the landscape, where the sandy lens is present, may receive greater water flows due to higher hydraulic conductivity than the less-permeable clay loam or SiC layers that borders them

(Concret, 1981; Revel, 1982). The decarbonation of the top soil in SL, added to the underlying redoximorphic features, reveal greater water transfer than in the EM profile, due to the underlying sandy lens. The marks within the SL profile imply an intense waterlogging due to prolonged soil saturation in winter. Moreover, we found that the Ck sublayer is Fe-poor; resulting in the sequence of a redoximorphic layer overlying a Fe-poor layer, which is the opposite of what is typically found in stagnic soils (IUSS Working Group WRB, 2022). Stagnic properties are commonly caused by downward rainwater. In the present SL profile however, intermittent groundwater upwelling also results in stagnic properties, with an inverse distribution of hydromorphic features.

In contrast, due to lower leaching of CaCO_3 in the top-hill, the EM profile remains calcareous on the surface. These high carbonate contents in the A horizon are evidence of the rejuvenation of the soil surface by the erosion process, very intense at this level of the slope. Within this profile, the granulometric clays and sands rates decrease progressively in favor of highly carbonated silts of the underlying Ck horizon (Figure 13).

At the bottom of the slope, the RS profile presents homogeneous physicochemical properties whatever the depth, remaining similar to SL and EM topsoils. This suggests that this profile results mainly from the accumulation of deposits

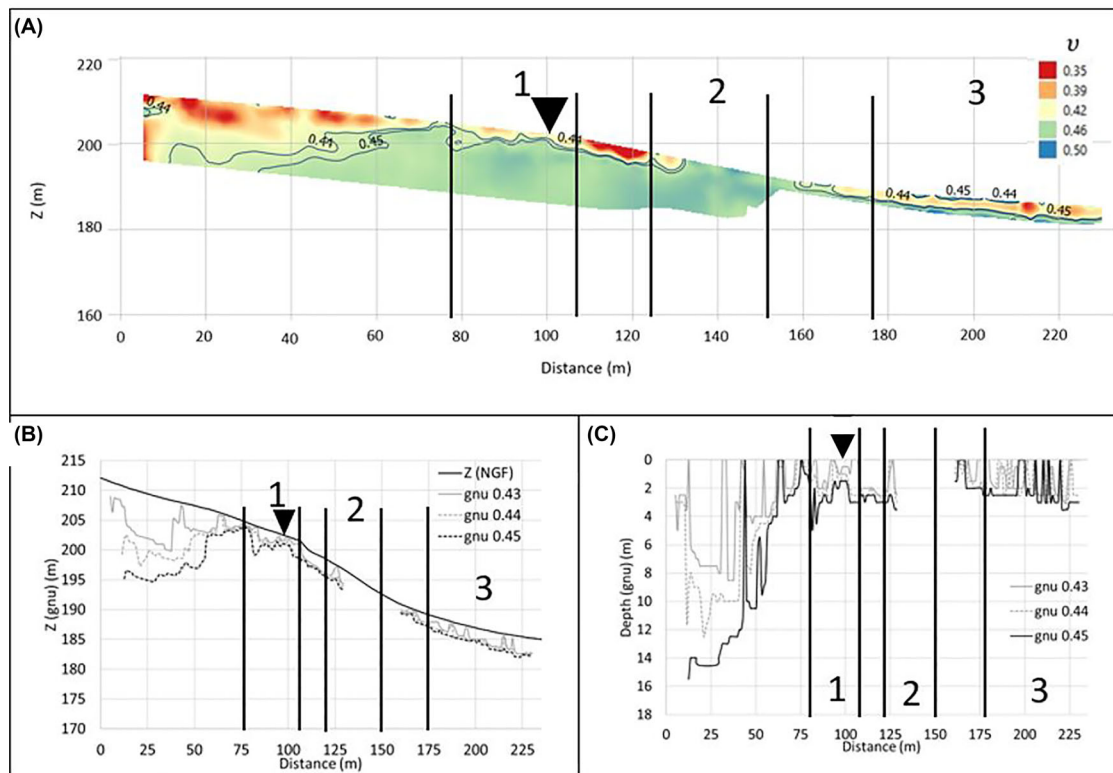


FIGURE 12 Poisson ratio versus topography (A and B) and versus depth (C) determined by seismic prospecting along the embankment-riverside (EM-RS) transect (▼: EM point, 1|1|2|1|3: areas of high ν associated with the rise of compact material described in Figure 11).

brought by colluvium and by tillage in the direction of the slope (Guiesse & Revel, 1995). The vicinity of the stream triggers an upwelling of groundwater, causing gleyic properties, which is a hallmark of such conditions (IUSS Working Group WRB, 2022).

Our XRD analyses show that the most abundant clay minerals are expansive clay minerals, like smectites and illite/smectite mixed-layered minerals, which is consistent with data from Gandois et al. (2011). These clay minerals swell following adsorption of water in interlayer and between layers, significantly impacting hydraulic conductivity. Smectites and illite/smectite mixed-layers have very low hydraulic conductivities in the range of 10^{-9} – 10^{-11} m/s (Benson & Trast, 1995). Their abundance in the clay fraction of most soil layers (25%–45% depending on the profile) can lead to low or very low hydraulic conductivities. The combined effect of a large proportion of clay fraction and the abundance of swelling clay minerals leads to (i) macroscopic swelling and closure of meso- and macroporosity when the soil water content increases during the saturation phase and (ii) high water holding capacities (Trochon et al., 2021). Due to a mixed Mediterranean and oceanic influence, contrasting climatic conditions on the study site enhance shrinkage and swelling properties. The limestone makes the clay highly saturated in calcium, which implies a good structuring and well-expressed shrink-swell properties (Hillel, 1998). This

impacts pore space geometry and thereby soil water saturation prior to waterlogging events.

4.2 | Heterogeneous molassic deposits in a hilly morphology enhance local waterlogging

The vertical and horizontal variations of V_p on the transect in Figure 11 show very strong heterogeneities within the molassic deposit, resulting from the juxtaposition of compact material with high V_p (Figure 11A) with unconsolidated zones where V_p is much lower, at the same depth.

According to Poisson's ratio values (ν), the water table downhill of EM is relatively shallow in October, at the end of the low-water period, when the stream is solely fed by groundwater (Figure 12). The surface layers in the area at the bottom of the plot are less consolidated, with a compact level between 1 and 3 m, according to the propagation speed of the P-waves (Figure 11). A rise in the water table level during the recharge phase can therefore lead it to connect to more permeable layers within the molassic deposit, such as the SLs (SL profile). Flows then converge in these locally more permeable environments. The seismic survey provides qualitative information on the hydraulic conductivity of the sedimentary layers (which is inversely related to V_p) and on the topography of the water table. This provides an estimate of the

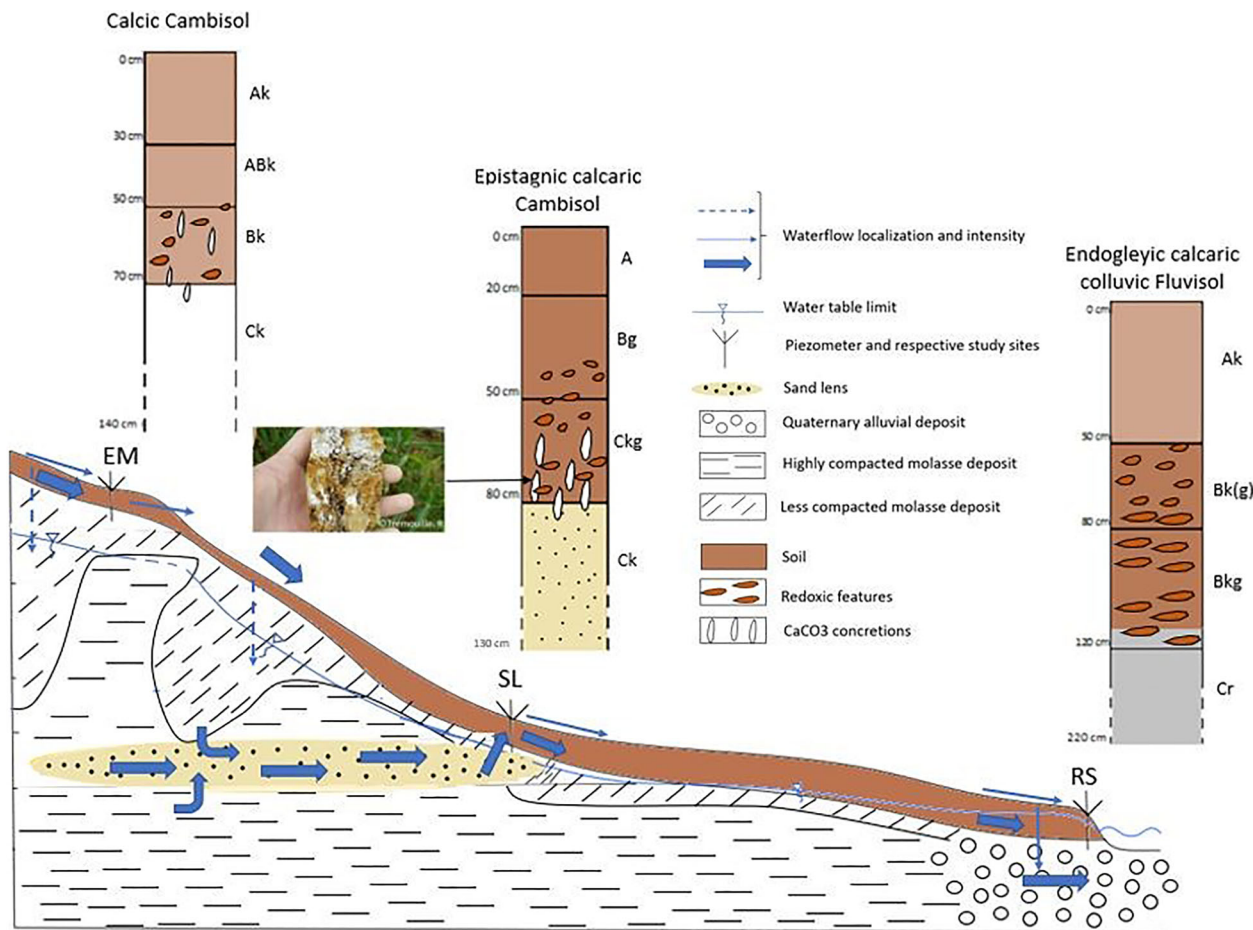


FIGURE 13 Conceptual scheme of the different types of water pathways identified in the soils of the Molassic Hills.

hydraulic gradient. Underground flows are most dynamic in areas where high transmissivity layers (low V_p) become saturated. This phenomenon occurs at the bottom of the slope, where upstream flows concentrate. By contrast, in the upper part of the hill, seismic geophysics highlights saturation levels that are completely independent of topography, with a collapse of the compact level creating some areas with strong piezometric depressions, as illustrated in Figure 13.

The processing of fine resolution topographic data, RGE ALTI with a 5 m resolution digital elevation model (DEM), enables to compute a topographic index known as Beven's index (Beven & Kirkby, 1979) (Figure 14), established according to a multidirectional circulation scheme. Identifying the area with the highest Beven's index value theoretically indicates where the water table is closest to the surface. In our case, the Beven index mainly highlights the existence of preferential flow paths within the plot (Figure 14). There are numerous preferential flow paths on the soil surface, separated by about 150 to 200 m, and connected to the watercourse (blue areas with arrows in Figure 14). The formation of these depressed areas, in a morphogenic context, can contribute to concentrate the runoff and recharge of the underground water

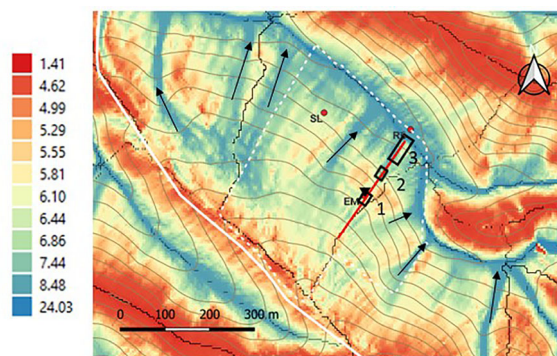


FIGURE 14 Beven index determined with a 5 m digital elevation model (DEM). The contour lines are spaced at 5 m (▼: position of embankment [EM] point, |||||: delimitation of areas on transect described in Figures 11 and 12).

reservoirs in a relatively limited space. Irregularities in the water table, caused by the variable depth of the compact level (Figures 11 and 12), are removed by heavy rainfall, before a horizontal water circulation can be initiated: This is the beginning of the saturation phase (Figure 6).

4.3 | A conceptual scheme of the different flows in the landscape

The different results obtained on the soils from the study sites allow the creation of a conceptual scheme of the water circulation patterns in the toposequence. This scheme (Figure 13), the representative of the water flows in the molassic hills of the studied region, takes the form of a transect with the three points RS, SL, and EM, characteristic of three different hydrological flows in the studied toposequence.

The RS point is close to the stream on deep soil with low carbonate content, homogeneous texture, and soil properties, in an overlying alluvium with a relatively high hydraulic conductivity. The low slope at this point implies that alluvial groundwater is mainly drained by the stream. This explains the holding of the water table above the stream water level throughout the year. Permanent deep waterlogging promotes reducing conditions and results in gleyic properties marked by a 100% gray color in soil from a depth of 120 cm, indicating a Cr horizon (Figure 13). After the summer, in September, the level of the water table is at its lowest (depth of 120 cm) due to low rainfall and sustained ETR. Significant nychthemeral fluctuations in the water table levels were recorded in September 2020, July, August, and September 2021 (high vertical daily variations, visible on Figure 8A), probably caused by riparian vegetation water uptake (tree alignments are present along the entire length of the watercourse). During these months, the stream is only fed by its alluvial water table.

During 4 months from December to late March-beginning of April, the water level in the SL piezometer (Figure 8) turns from a dry phase to a saturation phase, with water resurgence at the soil surface. The clayey texture in the first 60 cm at the SL point, in A and Bg horizon (Figure 3), and the high proportion of swelling clay minerals in this fraction (Figure 4) result in a low hydraulic conductivity of the soil. The high sand content at depth indicates the presence of a local SL, as frequently observed in the watershed (Concaret, 1981; Revel, 1982; Ferrant et al., 2011). During the saturation phase, when groundwater recharge and lateral circulation are effective, a connection to the SL is established when the water table rises through the most permeable layers of the molassic deposit. The SL then collects and drains the groundwater coming from uphill in a continuous flow. The SL point is located at the top of this lens, near the contact point between a sandy level and a clayey level with very low permeability. This discontinuity triggers water resurgence by enhancing water pressure in the SL. Even though the horizon above the SL is more clayey, the pressure put on the water in the lens by the continuous flow makes it resurge vertically and pass through any porosity available. In sum, the lens acts as a captive water table during the saturation phase. In January and February, although the water level remains at the soil surface in the SL piezometer, it evolves with very high amplitudes in the

EM one, depending on rainfall. The hydrological pathways involved are (i) the so-called return flow, reflecting an upward groundwater flow at the SL point and (ii) the so-called hypodermic flow, reflecting a more usual subsurface flow at the EM point, resulting directly from rainfall (Hewlett & Hibbert, 1963; Lee et al., 2020). The water resurgence is marked on the SL profile at a depth of 50–60 cm via the Ckg horizon, which has much more redoximorphic features than the other profiles with low permeability (Figure 12). This resurgence works in two phases. Firstly, a lack of deep groundwater recharge causes a dry phase with no flow. Secondly, inflow from the SL connects to the surface soil layers and leads to strong hypodermic and surface flows by resurgence, thereby causing a waterlogged phase. These flows are driven both by the specific topography and by the impermeable clayey layer that hinders water infiltration (Figures 1 and 14). During winter, runoff and hypodermic flow, also called subsurface runoff, favor rapid soil water movement. During this period, from December to end of March, the nychthemeral variations (Figures 8A and 10) of the SL water level are probably due to the daily water uptake by wheat growing in the plot. From April 2021 onward, the groundwater level in SL strongly drops. The tensiometric monitoring in the soil profile located above the SL (Figure 10), however, indicates that the soil remains saturated 1 month later (until the middle of June). Water is progressively taken up by the crops, leading to a progressive drying of the soil (Figures 6, 8–10).

The EM piezometer is located immediately uphill of a slope break, in an elevated topographic position compared to the other two monitored points. The seismic refraction tomography shows that above this point, the slope of the saturated level no longer follows the topographic slope and forms piezometric depressions, some of which are very deep (Figures 12 and 13). This specific configuration prevents groundwater circulation. The water table fluctuations observed at the EM point occur during major rainfall events and are mainly due to runoff after the soil recharge phase. Discharge is generally fast thereafter, as there is no inflow to maintain the water level in the soil. In addition, the proximity of a steep slope break accelerates the drainage of the saturated soil. During the winter period, the saturation of the subsoil does not completely reach the topsoil as it may be the case for the SL. From February 13, 2021, in the absence of rainfall, the water level in the EM piezometer progressively drops until it dries up completely. The SL point follows the same trend but dries up 3 months later (Figure 8A). According to the piezometric monitoring, the EM point does not really have a deep-water flow, or at least not at 140 cm depth. As a result, redoximorphic features of the Bk horizon are less distinct than in the other profiles. These features could be mainly due to an overall lack of permeability in the underlying Ck horizon which is compact limestone (Figure 13). This level of massive limestone accumulation at a depth of 70 cm is confirmed by seismic

prospection that highlights a compact zone ($V_p = 2000$ m/s) just below the EM point (Figure 11B). In sum, the flow at this point is mainly hypodermic, notably by the natural drainage provided by the break in the slope.

To go further and fully validate the flow patterns discussed here, both on a local and larger scale, it would be valuable to integrate saturated hydraulic conductivity values of the different soil layers. The use of quantitative measurements of soil hydrodynamic properties would enable modeling of flow patterns using a semi-distributed approach, such as TOPMODEL (Beven & Kirkby, 1979; Ambroise, Beven, et al., 1996; Ambroise, Freer, et al., 1996) or a spatially explicit approach (e.g., DHSVM, Wigmosta et al., 1994; Wigmosta & Lettenmaier, 1999). In addition, the different phases show different responses to extreme rainfall event (Figures 6 and 7A). Modeling the watershed response to these kinds of event throughout the year could also be pursued, for example, through an instantaneous unit hydrograph (Ünver & Mays, 1984). These modeling approaches would allow us to validate our assumptions about hydrological processes, using data recorded at the catchment outlet, the DEM, soil data, and in situ measurements of hydrodynamic properties.

5 | CONCLUSION

In this paper, we analyze soil data and hydrological monitoring, with the aim of conceptualizing the typical water flow paths of clayey calcisols in the molassic hills of southwestern France. We identify the areas where the waterlogging risk is the highest. This work highlights the major role of soils in the response of the stream to rainfall events. Indeed, a phase of soil recharge estimated around 100 mm of effective rain is necessary before the drainage season really begins. This can be considered the saturation of the soil mesoporosity. Moreafter, in the spring and summer, in the absence of significant rainfall events, the soils provide about 100 mm of water for crops. The soil porosity is filled before the drainage phase and supplies water during the water deficit phase. Despite climatic variability between successive hydrological years, the soil porosity remains stable around a value of 100 mm for the last 12 years. Mesoporosity plays a key role, filling up in the fall and emptying out in the spring. Our observations reveal three typical local water flow patterns occurring during the saturation phase in the studied soils, that can probably occur also in many other places of the catchment: (i) A perennial alluvial groundwater is established in the deeper, homogeneous, and permeable soils with proximity to the stream draining the groundwater table; (ii) groundwater feeds deep-lying most permeable SLs that locally saturate the profile and establish hypodermic and surface flows; and (iii) finally, the third mode of rain water circulation consists in a subsurface lateral flow and runoff which are not connected to the permanent water

table. The occurrence of these rapid soil water movements depends closely on the morphological configuration of the landscape, with local differences in uphill contributing area, slope, and flux convergence at the talweg.

The seismic refraction tomography revealed very strong heterogeneities at depth in the molassic deposit, with strata of high compactness saturated with water. The juxtaposition of compact layers with unconsolidated layers constitutes discontinuities that delineate the potential for groundwater storage and water circulation. Furthermore, at the bottom of the hill, the water table slope appears to be the same as the topographic slope, suggesting a vertical connection between the saturated and unsaturated soil layers, which is not the case at the top of the hill. We found that the areas with a high waterlogging potential may present (i) a mainly morphological determinism linked to the surface and subsurface runoff and (ii) a rather geological determinism at the lower part of the hill, associated with the location of SLs that trigger water resurgence. Our objective is to contribute to a reliable and predictive identification of areas at risk of waterlogging in molassic soils. This is particularly relevant for digital farming solutions, crop yield improvement, and reduction of GHGs emissions. In addition, our study could also help understand the evolution of streams that have a longer dry period due to climate change (Fovet et al., 2021). The work done here can be reproduced on other watersheds if they are equipped for hydrological monitoring. Other watersheds in the OZCAR network, with contrasting climates, could be valuable study areas. Note, however, that it might be worth simplifying the methodology used in this paper for the clay fraction analysis. Indeed, the clay composition could be partially inferred from a complete physicochemical analysis of the soil by granulometry coupled with a detailed CEC and geotechnical test. New low-cost probes could also facilitate field monitoring. To identify areas at risk of waterlogging on a larger scale, our approach could benefit from an innovative coupling of our hydrological scheme with aerial observations or even with satellite imagery. Indeed, synthetic aperture radar or multi-spectral imagery provides information about surface water patterns, soil moisture content, vegetation health, and land use/land cover.

AUTHOR CONTRIBUTIONS

Benjamin Trochon: Writing—original draft; writing—review and editing; conceptualization; methodology; formal analysis; investigation; validation. **Vincent Bustillo:** Writing—original draft; conceptualization; methodology; formal analysis; investigation; resources; data curation; supervision; validation. **Laurent Caner:** Formal analysis; methodology; resources; software; writing—review and editing. **Sylvain Pasquet:** Formal analysis; investigation; methodology; resources; writing—review and editing. **Virginie Suc, Franck Granouillac:** Data curation; investigation;

resources. **Anne Probst, Tiphaine Tallec:** Data curation; resources; writing—review and editing. **Jean-Luc Probst:** Data curation; resources. **Maritxu Guïresse:** Conceptualization; formal analysis; funding acquisition; methodology; project administration; resources; supervision; validation; writing—original draft; writing—review and editing.

ACKNOWLEDGMENTS

We would like to thank the technical staff of the analytical analysis platform of the functional ecology and environment laboratory, the technical staff of the soil analysis laboratory of Arras, and the “Groupement des Agriculteurs de la Gascogne Toulousaine” (GAGT) for facilitating access to the Montoussé catchment with a special thanks to M. Valero, owner of the parcel. Our thanks also go to Remi Tremouille for his help in the field and in the laboratory, to T. Camboulive, J. Desaying, N. Ferroni, B. Lemaire, and F. Ulloa-Cedamano for their contribution to the geophysical field campaign, and to D. Payandi-Rolland for his contribution to the validation of outlet hydrological data. We are grateful to the Occitanie Region for its contribution to the funding of this work and to the French Research Infrastructure OZCAR (Observatory of the Critical Zone: <http://www.ozcar-ri.org/>) for supporting the Montoussé catchment hydrochemical survey. We also thank the anonymous reviewers for their valuable comments, which helped improve the manuscript. This study was co-founded by French Ministry of Agriculture and Occitanie Region subsidies.

CONFLICT OF INTEREST STATEMENT

The authors declare having no conflicts of interest.

ORCID

Jean-Luc Probst  <https://orcid.org/0000-0002-1295-5264>
Maritxu Guïresse  <https://orcid.org/0000-0002-2617-9876>

REFERENCES

- Alías, L. J., López-Bermúdez, F., Marín-Sanleandro, P., Romero-Díaz, M. A., & Martínez, J. (1997). Clay minerals and soil fertility loss on Petric Calcisol under a semiarid Mediterranean environment. *Soil Technology*, *10*(1), 9–19. [https://doi.org/10.1016/0933-3630\(95\)00044-5](https://doi.org/10.1016/0933-3630(95)00044-5)
- Amanieu, R., Ambert, P., Babonaux, Y., Seronde-Babonaux, A.-M., Baby, F., Jean-Louis, B., Barathon, J.-J., Barthélémy, L., Beaudet, G., Bertrand, G., Bertrand, C., De Bolos I Capdevilla, M., Bomer, B., Bousquet, B., De Brum Ferreira, A., Calvet, M., Carcenac, C., Cavaillé, A., Chaput, J.-L., ... Wolff, P. (1984). *Montagnes & Piémonts*. CNRS.
- Ambroise, B., Beven, K., & Freer, J. (1996). Toward a generalization of the TOPMODEL concepts: Topographic indices of hydrological similarity. *Water Resources Research*, *32*(7), 2135–2145. <https://doi.org/10.1029/95WR03716>
- Ambroise, B., Freer, J., & Beven, K. (1996). Application of a generalized TOPMODEL to the small Ringelbach catchment, Vosges, France. *Water Resources Research*, *32*(7), 2147–2159. <https://doi.org/10.1029/95WR03715>
- Benson, C. H., & Trast, J. M. (1995). Hydraulic conductivity of thirteen compacted clays. *Clays and Clay Minerals*, *43*(6), 669–681. <https://doi.org/10.1346/CCMN.1995.0430603>
- Bernot, J. (1961). *Contribution à l'étude des sols lessivés des terrasses de la Garonne* [Doctoral thesis]. University of Toulouse.
- Beven, K. J., & Kirkby, M. J. (1979). A physically based, variable contributing area model of basin hydrology. *Hydrological Sciences*, *24*, 27.
- Bouma, J. (1981). Soil survey interpretation: Estimating use-potentials of a clay soil under various moisture regimes. *Geoderma*, *26*(3), 165–177. [https://doi.org/10.1016/0016-7061\(81\)90013-6](https://doi.org/10.1016/0016-7061(81)90013-6)
- Bouzigues, R., Favrot, J. C., Chossat, J. C., & Voltz, M. (1998). Effect of the structural organization of stagnic luvisols on drainage outflow. *Canadian Journal of Soil Science*, *78*(4), 631–641. <https://doi.org/10.4141/S97-017>
- Bouzigues, R., Ribolzi, O., Favrot, J. C., & Valles, V. (1997). Carbonate redistribution and hydrogeochemical processes in two calcareous soils with groundwater in a Mediterranean environment. *European Journal of Soil Science*, *48*(2), 201–211. <https://doi.org/10.1111/j.1365-2389.1997.tb00541.x>
- Bouzigues, R., & Vinas, A. (1989). *Identification des différents faciès structuraux dans les horizons argilliques des sols de Boulbènes: Conséquences sur les transferts hydriques*. INRA.
- Bur, T. (2008). *Impact anthropique sur les éléments traces métalliques dans les sols agricoles de Midi-Pyrénées. Implications en termes de limites et de charges critiques* [Doctoral thesis]. University of Toulouse. <https://www5.obs-mip.fr/wp-content-omp/uploads/sites/8/2016/09/bur-1.pdf>
- Calvet, M., Gunnell, Y., & Laumonier, B. (2021). Denudation history and palaeogeography of the Pyrenees and their peripheral basins: An 84-million-year geomorphological perspective. *Earth-Science Reviews*, *215*, 103436. <https://doi.org/10.1016/j.earscirev.2020.103436>
- Caner, L., & Hubert, F. (2012). Développements actuels dans l'identification et la quantification des minéraux argileux des sols. *Etude et Gestion des Sols*, *19*, 249–261.
- Canérot, J. (2008). *Les Pyrénées*. Atlantica.
- Casal, L., Durand, P., Akkal-Corfini, N., Benhamou, C., Laurent, F., Salmon-Monviola, J., Ferrant, S., Probst, A., Probst, J.-L., & Vertès, F. (2019). Reduction of stream nitrate concentrations by land management in contrasted landscapes. *Nutrient Cycling in Agroecosystems*, *114*(1), 1–17. <https://doi.org/10.1007/s10705-019-09985-0>
- Cerdà, A. (1996). Soil aggregate stability in three Mediterranean environments. *Soil Technology*, *9*(3), 133–140. [https://doi.org/10.1016/S0933-3630\(96\)00008-6](https://doi.org/10.1016/S0933-3630(96)00008-6)
- Chaumet, B., Probst, J. L., Eon, P., Payré-Suc, V., Granouillac, F., Camboulive, T., Riboul, D., Pautot, C., Tavella, M. J., Trochon, B., & Probst, A. (2021). Pesticide distribution in pond sediments from an agricultural catchment (Auradé, SW France). *Environmental Sciences Proceedings*, *7*(1), 13. <https://doi.org/10.3390/ECWS-5-08184>
- Ciesielski, H., Sterckeman, T., Santerne, M., & Willery, J. P. (1997). Determination of cation exchange capacity and exchangeable cations in soils by means of cobalt hexamine trichloride. Effects of experimental conditions. *Agronomie*, *17*(1), 1–7. <https://doi.org/10.1051/agro:19970101>
- CITEPA. (2020). Gaz à effet de serre. In *Inventaire des émissions de polluants atmosphériques et de gaz à effet de serre en France-Format Secten* (pp. 105–110). CITEPA.
- Concaret, J. (1981). *Drainage agricole: Théorie et pratique*. Chambre Régionale d'Agriculture de Bourgogne.

- Favrot, J. C., Bouzigues, R., Valles, V., & Tessier, S. (1992). Contrasting structures in the subsoil of the Boulbènes of the Garonne basin, France. *Geoderma*, 53, 13.
- Ferrant, S., Bustillo, V., Burel, E., Salmon-Monviola, J., Claverie, M., Jarosz, N., Yin, T., Rivalland, V., Dedieu, G., Demarez, V., Ceschia, E., Probst, A., Al-Bitar, A., Kerr, Y., Probst, J.-L., Durand, P., & Gascoïn, S. (2016). Extracting soil water holding capacity parameters of a distributed agro-hydrological model from high resolution optical satellite observations series. *Remote Sensing*, 8(2), 154. <https://doi.org/10.3390/rs8020154>
- Ferrant, S., Oehler, F., Durand, P., Ruiz, L., Salmon-Monviola, J., Justes, E., Dugast, P., Probst, A., Probst, J.-L., & Sanchez-Perez, J.-M. (2011). Understanding nitrogen transfer dynamics in a small agricultural catchment: Comparison of a distributed (TNT2) and a semi distributed (SWAT) modeling approaches. *Journal of Hydrology*, 406(1–2), 1–15. <https://doi.org/10.1016/j.jhydrol.2011.05.026>
- Fovet, O., Belemtougri, A., Boithias, L., Braud, I., Charlier, J. B., Cottet, M., Daudin, K., Dramais, G., Ducharne, A., Folton, N., Grippa, M., Hector, B., Kuppel, S., Le Coz, J., Legal, L., Martin, P., Moatar, F., Molénat, J., Probst, A., ... Detry, T. (2021). Intermittent rivers and ephemeral streams: Perspectives for critical zone science and research on socio-ecosystems. *WIREs Water*, 8(4), e1523. <https://doi.org/10.1002/wat2.1523>
- Gaillardet, J., Braud, I., Hankard, F., Anquetin, S., Bour, O., Dorfliger, N., de Dreuzy, J. R., Galle, S., Galy, C., Gogo, S., Gourcy, L., Habets, F., Laggoun, F., Longuevergne, L., Le Borgne, T., Naaim-Bouvet, F., Nord, G., Simonneaux, V., Six, D., ... Zitouna, R. (2018). OZCAR: The French network of critical zone observatories. *Vadose Zone Journal*, 17(1), 180067. <https://doi.org/10.2136/vzj2018.04.0067>
- Gandois, L., Perrin, A. S., & Probst, A. (2011). Impact of nitrogenous fertiliser-induced proton release on cultivated soils with contrasting carbonate contents: A column experiment. *Geochimica et Cosmochimica Acta*, 75(5), 1185–1198. <https://doi.org/10.1016/j.gca.2010.11.025>
- Grimaldi, M., & Tessier, D. (1986). Changements des propriétés de retrait, de gonflement et de rétention d'un matériau limoneux soumis à un compactage dynamique. *Science du sol*, 24(4), 319–336.
- Guirresse, M., & Bourgeat, F. (1991). Experimentation en sols de Boulbènes: Efficacité d'un réseau de drainage et caractéristiques des sols. *CEMAGREF, Hydraulique Agricole*, 10, 63–87.
- Guirresse, M., & Revel, J. C. (1995). Erosion due to cultivation of calcareous clay soils on hillsides in south-west France. II. Effect of ploughing down the steepest slope. *Soil and Tillage Research*, 35(3), 157–166. [https://doi.org/10.1016/0167-1987\(95\)00483-1](https://doi.org/10.1016/0167-1987(95)00483-1)
- Hartmann, P., Zink, A., Fleige, H., & Horn, R. (2012). Effect of compaction, tillage and climate change on soil water balance of Arable Luvisols in Northwest Germany. *Soil and Tillage Research*, 124, 211–218. <https://doi.org/10.1016/j.still.2012.06.004>
- Hewlett, J. D., & Hibbert, A. R. (1963). Moisture and energy conditions within a sloping soil mass during drainage. *Journal of Geophysical Research*, 68(4), 1081–1087. <https://doi.org/10.1029/JZ068i004p01081>
- Hillel, D. (1998). *Environmental soil physics*. Academic Press.
- Hoorn, C., Guerrero, J., Sarmiento, G. A., & Lorente, M. A. (1995). Andean tectonics as a cause for changing drainage patterns in Miocene northern South America. *Geology*, 23(3), 237. [https://doi.org/10.1130/0091-7613\(1995\)023<0237:ATAACF>2.3.CO;2](https://doi.org/10.1130/0091-7613(1995)023<0237:ATAACF>2.3.CO;2)
- Hu, Z., Zhang, J., Li, S., Xie, H., Wang, J., Zhang, T., Li, Y., & Zhang, H. (2010). Effect of aeration rate on the emission of N₂O in anoxic-aerobic sequencing batch reactors (A/O SBRs). *Journal of Bioscience and Bioengineering*, 109(5), 487–491. <https://doi.org/10.1016/j.jbiosc.2009.11.001>
- Hubert, F., Caner, L., Meunier, A., & Lanson, B. (2009). Advances in characterization of soil clay mineralogy using X-ray diffraction: From decomposition to profile fitting. *European Journal of Soil Science*, 60(6), 1093–1105. <https://doi.org/10.1111/j.1365-2389.2009.01194.x>
- Hubschman, J. (1975). I. —Modèles et formations quaternaires du terrefort molassique, au Sud de Toulouse. *Bulletin de l'Association française pour l'étude du quaternaire*, 12(3), 125–136. <https://doi.org/10.3406/quate.1975.1260>
- IUSS Working Group WRB. (2022). *World reference base for soil resources. International soil classification system for naming soils and creating legends for soil maps* (4th ed.). International Union of Soil Sciences (IUSS).
- Jacquin, F., Cheloufi, H., & Vong, P. C. (1992). Immobilization and mineralization kinetics of a nitrogen fertilizer in calcareous clayey soil (rendzina). *Science of the Total Environment*, 117–118, 271–278. [https://doi.org/10.1016/0048-9697\(92\)90094-9](https://doi.org/10.1016/0048-9697(92)90094-9)
- Janeau, J. L., Gillard, L. C., Grellier, S., Jouquet, P., Le, T. P. Q., Luu, T. N. M., Ngo, Q. A., Orange, D., Pham, D. R., Tran, D. T., Tran, S. H., Trinh, A. D., Valentin, C., & Rochelle-Newall, E. (2014). Soil erosion, dissolved organic carbon and nutrient losses under different land use systems in a small catchment in northern Vietnam. *Agricultural Water Management*, 146, 314–323. <https://doi.org/10.1016/j.agwat.2014.09.006>
- Kodešová, R., Jirků, V., Kodeš, V., Mühlhanslová, M., Nikodem, A., & Žigová, A. (2011). Soil structure and soil hydraulic properties of Haplic Luvisol used as arable land and grassland. *Soil and Tillage Research*, 111(2), 154–161. <https://doi.org/10.1016/j.still.2010.09.007>
- Lagacherie, P., Snee, A.-R., Gomez, C., Bacha, S., Coulouma, G., Hamrouni, M. H., & Mekki, I. (2013). Combining Vis-NIR hyperspectral imagery and legacy measured soil profiles to map subsurface soil properties in a Mediterranean area (Cap-Bon, Tunisia). *Geoderma*, 209–210, 168–176. <https://doi.org/10.1016/j.geoderma.2013.06.005>
- Lanson, B. (1997). Decomposition of experimental X-ray diffraction patterns (profile fitting): A convenient way to study clay minerals. *Clays and Clay Minerals*, 45(2), 132–146. <https://doi.org/10.1346/CCMN.1997.0450202>
- Lee, R. M., McGuire, K. J., Strahm, B. D., Knoepp, J. D., Jackson, C. R., & Stewart, R. D. (2020). Revisiting the Hewlett and Hibbert (1963) hillslope drainage experiment and modeling effects of decadal pedogenic processes and leaky soil boundary conditions. *Water Resources Research*, 56(1), e2019WR025090. <https://doi.org/10.1029/2019WR025090>
- Legros, J. P. (2007). *Les grands sols du monde*. Presses polytechniques et universitaires romandes.
- Lucas, Y., & Vaute, L. (2011). Approche spatialisée dans la modélisation hydrogéologique d'un ancien secteur minier. *Revue des sciences de l'eau*, 24(1), 77–85. <https://doi.org/10.7202/045829ar>
- Macary, F., Dias, J. A., Uny, D., & Probst, A. (2013). Assessment of the effects of best environmental practices on reducing pesticide contamination in surface water, using multi-criteria modelling combined with a GIS. *International Journal of Multicriteria Decision Making*, 3(2/3), 178. <https://doi.org/10.1504/IJMCDM.2013.053725>

- Mekki, I., Zitouna Chebbi, R., Jacob, F., Ben Mechlia, N., Prevot, L., Albergel, J., & Voltz, M. (2018). Impact of land use on soil water content in a hilly rainfed agrosystem: A case study in the Cap Bon peninsula in Tunisia. *Agroforestry*, 3(1), 64–74. <https://doi.org/10.7251/AGRENG1801064M>
- Meyer, R., & Guillet, B. (1980). Faciès différenciés d'origine pédologique dans la molasse oligo-miocène d'Aquitaine centrale. *Sciences Géologiques: Bulletin*, 33(2), 67–80. <https://doi.org/10.3406/sgeol.1980.1572>
- Michel, J. C., & Tessier, D. (2003). Comportement et organisation de sols de Boulbène dans le Tarn. *Étude et Gestion des Sols*, 10, 71–80.
- Moore, D. M., & Reynolds, R. C., Jr. (1997). *X-ray diffraction and the identification and analysis of clay minerals* (2nd ed.). Oxford University Press (OUP).
- Paegelow, M., Decroux, J., Hubschman, J., & Puginier, M. (1991). *Des mesures simples d'aménagement rural contre la pollution par les nitrates: L'exemple d'Auradé (Gers, France)*. Nitrates, agriculture, eau.
- Pasquet, S., & Bodet, L. (2017). SWIP: An integrated workflow for surface-wave dispersion inversion and profiling. *Geophysics*, 82(6), WB47–WB61. <https://doi.org/10.1190/geo2016-0625.1>
- Pasquet, S., Bodet, L., Dhemaied, A., Mouhri, A., Vitale, Q., Rejiba, F., Flipo, N., & Guérin, R. (2015). Detecting different water table levels in a shallow aquifer with combined P-, surface and SH-wave surveys: Insights from VP/VS or Poisson's ratios. *Journal of Applied Geophysics*, 113, 38–50. <https://doi.org/10.1016/j.jappgeo.2014.12.005>
- Perrin, A.-S., Probst, A., & Probst, J.-L. (2008). Impact of nitrogenous fertilizers on carbonate dissolution in small agricultural catchments: Implications for weathering CO₂ uptake at regional and global scales. *Geochimica et Cosmochimica Acta*, 72(13), 3105–3123. <https://doi.org/10.1016/j.gca.2008.04.011>
- Podwojewski, P., Janeau, J. L., Grellier, S., Valentin, C., Lorentz, S., & Chaplot, V. (2011). Influence of grass soil cover on water runoff and soil detachment under rainfall simulation in a sub-humid South African degraded rangeland. *Earth Surface Processes and Landforms*, 36(7), 911–922. <https://doi.org/10.1002/esp.2121>
- Ponnou-Delaffon, V., Probst, A., Payre-Suc, V., Granouillac, F., Ferrant, S., Perrin, A.-S., & Probst, J.-L. (2020). Long and short-term trends of stream hydrochemistry and high frequency surveys as indicators of the influence of climate change, agricultural practices and internal processes (Aurade agricultural catchment, SW France). *Ecological Indicators*, 110, 105894. <https://doi.org/10.1016/j.ecolind.2019.105894>
- Pusch, R. (2006). Mechanical properties of clays and clay minerals. In *Developments in clay science* (Vol. 1, pp. 247–260). Elsevier. [https://doi.org/10.1016/S1572-4352\(05\)01006-8](https://doi.org/10.1016/S1572-4352(05)01006-8)
- Quijano, L., Kuhn, N. J., & Navas, A. (2020). Effects of interrill erosion on the distribution of soil organic and inorganic carbon in different sized particles of Mediterranean Calcisols. *Soil and Tillage Research*, 196, 104461. <https://doi.org/10.1016/j.still.2019.104461>
- Redon, P. O., Bur, T., Guisresse, M., Probst, J. L., Toiser, A., Revel, J. C., Jolivet, C., & Probst, A. (2013). Modelling trace metal background to evaluate anthropogenic contamination in arable soils of south-western France. *Geoderma*, 206, 112–122. <https://doi.org/10.1016/j.geoderma.2013.04.023>
- Revel, J. C. (1982). *Formation des sols sur marnes: Étude d'une chronoséquence et d'une toposéquence complexe dans le terrefort toulousain*. Institut National Polytechnique de Toulouse.
- Revel, J.-C., & Bourgeat, F. (1981). Sols fossiles du Terrefort toulousain. Leur signification paléoclimatique. *Bulletin de l'association française pour l'étude du quaternaire*, 3, 149–158.
- Revel, J.-C., Coste, N., Cavalie, J., & Costes, J.-L. (1989). Premiers résultats expérimentaux sur l'entraînement mécanique des terres par le travail du sol dans le Terrefort toulousain (France). *Cahiers ORSTOM: série pédologie*, XXV(1–2), 111–118.
- Revel, J. C., & Guisresse, M. (1995). Erosion due to cultivation of calcareous clay soils on the hillsides of south west France. I. Effect of former farming practices. *Soil and Tillage Research*, 35(3), 147–155. [https://doi.org/10.1016/0167-1987\(95\)00482-3](https://doi.org/10.1016/0167-1987(95)00482-3)
- Righi, D., Velde, B., & Meunier, A. (1995). Clay stability in clay-dominated soil systems. *Clay Minerals*, 30(1), 45–54. <https://doi.org/10.1180/claymin.1995.030.1.05>
- Roussiez, V., Probst, A., & Probst, J.-L. (2013). Significance of floods in metal dynamics and export in a small agricultural catchment. *Journal of Hydrology*, 499, 71–81. <https://doi.org/10.1016/j.jhydrol.2013.06.013>
- Rücker, C., Günther, T., & Wagner, F. M. (2017). pyGIMLI: An open-source library for modelling and inversion in geophysics. *Computers & Geosciences*, 109, 106–123. <https://doi.org/10.1016/j.cageo.2017.07.011>
- Ruellan, A. (1984). Les sols calcaires: Les principaux travaux des pédologues français. In *Livre jubilaire du cinquantenaire* (pp. 111–121). Association Française pour l'Étude du Sol.
- Salvador, M. M. S., Köhne, S., Köhne, J. M., Lennartz, B., & Libardi, P. L. (2011). Dye tracer and morphophysical properties to observe water flow in a Gleyic Luvisol. *Scientia Agricola*, 68(2), 160–166. <https://doi.org/10.1590/S0103-90162011000200005>
- Sandler, A. (2013). Clay distribution over the landscape of Israel: From the hyper-arid to the Mediterranean climate regimes. *Catena*, 110, 119–132. <https://doi.org/10.1016/j.catena.2013.05.016>
- Shalaby, A., Stüwe, K., Fritz, H., & Makroum, F. (2006). The El Mayah molasse basin in the Eastern Desert of Egypt. *Journal of African Earth Sciences*, 45(1), 1–15. <https://doi.org/10.1016/j.jafrearsci.2006.01.004>
- Smith, D. G., & Putnam, P. E. (1980). Anastomosed river deposits: Modern and ancient examples in Alberta, Canada. *Canadian Journal of Earth Sciences*, 17(10), 1396–1406. <https://doi.org/10.1139/e80-147>
- Solazzi, S. G., Bodet, L., Hollinger, K., & Jougnot, D. (2021). Surface-wave dispersion in partially saturated soils: The role of capillary forces. *Journal of Geophysical Research*, 1–18. <https://doi.org/10.1029/2021JB022074>
- Spaan, W. P., Sikking, A. F. S., & Hoogmoed, W. B. (2005). Vegetation barrier and tillage effects on runoff and sediment in an alley crop system on a Luvisol in Burkina Faso. *Soil and Tillage Research*, 83(2), 194–203. <https://doi.org/10.1016/j.still.2004.07.016>
- Taghavi, L., Probst, J. L., Merlina, G., Marchand, A. L., Durbe, G., & Probst, A. (2010). Flood event impact on pesticide transfer in a small agricultural catchment (Montoussé at Auradé, south west France). *International Journal of Environmental Analytical Chemistry*, 90(3–6), 390–405. <https://doi.org/10.1080/03067310903195045>
- Talleg, T., Béziat, P., Jarosz, N., Rivalland, V., & Ceschia, E. (2013). Crops' water use efficiencies in temperate climate: Comparison of stand, ecosystem and agronomical approaches. *Agricultural and Forest Meteorology*, 168, 69–81. <https://doi.org/10.1016/j.agrformet.2012.07.008>
- Tassinari, C., Lagacherie, P., Bouzigues, R., & Legros, J. P. (2002). Estimating soil water saturation from morphological soil indicators in a

- pedologically contrasted Mediterranean region. *Geoderma*, 108(3–4), 225–235. [https://doi.org/10.1016/S0016-7061\(02\)00132-5](https://doi.org/10.1016/S0016-7061(02)00132-5)
- Terefe, T., Mariscal-Sancho, I., Peregrina, F., & Espejo, R. (2008). Influence of heating on various properties of six Mediterranean soils. A laboratory study. *Geoderma*, 143(3–4), 273–280. <https://doi.org/10.1016/j.geoderma.2007.11.018>
- Tessier, D., Bouzigues, B., Favrot, J. C., & Valles, V. (1992). Influence du micro-relief sur l'évolution texturale des argiles dans les sols lessivés de la vallée de la Garonne. Différenciation des structures verticales ou prismatiques. *C. R. Académie des Sciences de Paris*, 315, 1027–1032.
- Trochon, B., Caner, L., Bustillo, V., & Guisresse, M. (2021, August 23–27). *Impact of clay mineralogy in the development of waterlogging and shrinkage cracks in clay-limestone soils in France south-west* [Conference presentation]. Eurosoil 2021: Connecting people and soil. Virtual.
- Ünver, O., & Mays, L. W. (1984). Optimal determination of loss rate functions and unit hydrographs. *Water Resources Research*, 20(2), 203–214. <https://doi.org/10.1029/WR020i002p00203>
- Valentin, C., Agus, F., Alamban, R., Boosaner, A., Bricquet, J. P., Chaplot, V., de Guzman, T., de Rouw, A., Janeau, J. L., Orange, D., Phachomphonh, K., Phai, D. D., Podwojewski, P., Ribolzi, O., Silvera, N., Subagyono, K., Thiébaux, J. P., Toan, T. D., & Vadari, T. (2008). Runoff and sediment losses from 27 upland catchments in Southeast Asia: Impact of rapid land use changes and conservation practices. *Agriculture, Ecosystems & Environment*, 128(4), 225–238. <https://doi.org/10.1016/j.agee.2008.06.004>
- Van Lanen, H. A. J., Reinds, G. J., Boersma, O. H., & Bouma, J. (1992). Impact of soil management systems on soil structure and physical properties in a clay loam soil, and the simulated effects on water deficits, soil aeration and workability. *Soil and Tillage Research*, 23(3), 203–220. [https://doi.org/10.1016/0167-1987\(92\)90101-G](https://doi.org/10.1016/0167-1987(92)90101-G)
- Velde, B. (2001). Clay minerals in the agricultural surface soils in the Central United States. *Clay Minerals*, 36(3), 277–294. <https://doi.org/10.1180/000985501750539391>
- Wang, M., Hu, R., Ruser, R., Schmidt, C., & Kappler, A. (2020). Role of chemodenitrification for N₂O emissions from nitrate reduction in rice paddy soils. *ACS Earth and Space Chemistry*, 4(1), 122–132. <https://doi.org/10.1021/acsearthspacechem.9b00296>
- Wang, Z., Li, W., Wang, Q., Liu, S., Hu, Y., & Fan, K. (2019). Relationships between the petrographic, physical and mechanical characteristics of sedimentary rocks in Jurassic weakly cemented strata. *Environmental Earth Sciences*, 78(5), 131. <https://doi.org/10.1007/s12665-019-8130-6>
- Whalley, W. R., Jenkins, M., & Attenborough, K. (2012). The velocity of shear waves in unsaturated soil. *Soil and Tillage Research*, 125, 30–37. <https://doi.org/10.1016/j.still.2012.05.013>
- Wigmosta, M. S., & Lettenmaier, D. P. (1999). A comparison of simplified methods for routing topographically driven subsurface flow. *Water Resources Research*, 35(1), 255–264.
- Wigmosta, M. S., Vail, L. W., & Lettenmaier, D. P. (1994). A distributed hydrology-vegetation model for complex terrain. *Water Resources Research*, 30(6), 1665–1679. <https://doi.org/10.1029/94WR00436>
- Wojdyr, M. (2007). *Fityk 0.8. 2 free software*. Fityk Developers. <http://www.unipress.waw.pl/fityk>
- Wu, X., & Probst, A. (2021). Influence of ponds on hazardous metal distribution in sediments at a catchment scale (agricultural critical zone, S-W France). *Journal of Hazardous Materials*, 411, 125077. <https://doi.org/10.1016/j.jhazmat.2021.125077>
- Zimmer, D., Bouzigues, R., Chossat, J. C., Favrot, J. C., & Guisresse, M. (1991). Importance et déterminisme des infiltrations profondes en luvisols-redoxisols drainés. Incidence sur les modalités de drainage. *Science du sol*, 29(4), 321–337.

How to cite this article: Trochon, B., Bustillo, V., Caner, L., Pasquet, S., Suc, V., Granouillac, F., Probst, A., Probst, J.-L., Tallec, T., & Guisresse, M. (2023). Main water pathways in cultivated clayey calcisols in molassic hills in southwestern France: Toward spatialization of soil waterlogging. *Vadose Zone Journal*, 22, e20272. <https://doi.org/10.1002/vzj2.20272>